MNRAS **479**, 2547–2563 (2018) Advance Access publication 2018 March 3 doi:10.1093/mnras/sty1541

# Characterizing circumgalactic gas around massive ellipticals at $z \sim 0.4$ – I. Initial results\*

Hsiao-Wen Chen, † Fakhri S. Zahedy, † Sean D. Johnson, 2,3 † ,‡ Rebecca M. Pierce, 1,4 Yun-Hsin Huang, Benjamin J. Weiner and Jean-René Gauthier Gauthier

Accepted 2018 June 6. Received 2018 April 09; in original form 2018 January 15

#### **ABSTRACT**

We present a new Hubble Space Telescope Cosmic Origins Spectrograph (COS) absorptionline survey to study halo gas around 16 luminous red galaxies (LRGs) at z = 0.21-0.55. The LRGs are selected uniformly with stellar mass  $M_{\rm star} > 10^{11} \, {\rm M}_{\odot}$  and no prior knowledge of the presence/absence of any absorption features. Based on observations of the full Lyman series, we obtain accurate measurements of neutral hydrogen column density  $N(H_1)$  and find that high-N(H<sub>I</sub>) gas is common in these massive quiescent haloes with a median of  $\langle \log N(\text{H I}) \rangle = 16.6$  at projected distances  $d \lesssim 160$  kpc. We measure a mean covering fraction of optically thick gas with log  $N(\text{H {\sc i}}) \gtrsim 17.2$  of  $\langle \kappa \rangle_{\text{LLS}} = 0.44^{+0.12}_{-0.11}$  at  $d \lesssim 160$  kpc and  $\langle \kappa \rangle_{\rm LLS} = 0.71^{+0.11}_{-0.20}$  at  $d \lesssim 100$  kpc. The line-of-sight velocity separations between the H<sub>I</sub> absorbing gas and LRGs are characterized by a mean and dispersion of  $\langle v_{\text{gas-gal}} \rangle = 29 \text{ km s}^{-1}$ and  $\sigma_{(v_{gas-gal})} = 171 \text{ km s}^{-1}$ . Combining COS far-ultraviolet and ground-based echelle spectra provides an expanded spectral coverage for multiple ionic transitions, from low-ionization MgII and Si II, to intermediate-ionization SiIII and C III, and to high-ionization O VI absorption lines. We find that intermediate ions probed by C III and Si III are the most prominent UV metal lines in LRG haloes with a mean covering fraction of  $\langle \kappa(C \parallel) \rangle_{0.1} = 0.75^{+0.08}_{-0.13}$  for  $W_r(977) \geqslant$ 0.1 Å at d < 160 kpc, comparable to what is seen for C III in  $L_*$  and sub- $L_*$  star-forming and red galaxies but exceeding Mg II or O VI in quiescent halos. The COS-LRG survey shows that massive quiescent haloes contain widespread chemically enriched cool gas and that little distinction between LRG and star-forming haloes is found in their HI and CIII content.

**Key words:** surveys – galaxies: elliptical and lenticular, cD – galaxies: formation – galaxies: haloes – intergalactic medium – quasars: absorption lines.

#### 1 INTRODUCTION

The circumgalactic medium (CGM), located in the space between galaxies and the intergalactic medium (IGM), is regulated by the

complex interaction between IGM accretion and stellar feedback. An accurate characterization of the CGM is therefore critical for understanding how galaxies grow and evolve. Previous analytical calculations and hydrodynamical simulations have suggested that chemically pristine gas accreted from the IGM by low-mass galaxies in less massive dark matter haloes ( $M_{\rm halo} \lesssim 10^{12} \, {\rm M}_{\odot}$ ) is cool and never shock-heated to the virial temperature of the dark matter halo, whereas more massive haloes acquire their gas through a hot channel in which the gas is shock-heated to temperatures  $T \gtrsim 10^6 \, {\rm K}$  (see Faucher-Giguère 2017 for a recent review and a list of references). At the same time, both cosmological simulations and observations of the high-redshift Universe have also highlighted the importance of supergalactic winds in enriching the CGM of star-

<sup>&</sup>lt;sup>1</sup>Department of Astronomy & Astrophysics, the University of Chicago, Chicago, IL 60637, USA

<sup>&</sup>lt;sup>2</sup>Department of Astrophysics, Princeton University, Princeton, NJ 08544, USA

<sup>&</sup>lt;sup>3</sup>The Observatories of the Carnegie Institution for Science, 813 Santa Barbara Street, Pasadena, CA 91101, USA

<sup>&</sup>lt;sup>4</sup>Department of Aerospace Engineering, University of Maryland, College Park, MD 20742, USA

<sup>&</sup>lt;sup>5</sup>Steward Observatory, University of Arizona, Tucson, AZ 85721, USA

<sup>&</sup>lt;sup>6</sup>DataScience.com, Culver City, CA 90230, USA

<sup>\*</sup> Based on data gathered with the 6.5 m Magellan Telescopes located at Las Campanas Observatory, the W. M. Keck Observatory, and the NASA/ESA *Hubble Space Telescope* operated by the Space Telescope Science Institute and the Association of Universities for Research in Astronomy, Inc., under NASA contract NAS 5-26555.

<sup>†</sup> E-mail: hchen@oddjob.uchicago.edu (H-WC); fsz@uchicago.edu (FSZ); sdj@astro.princeton.edu (SDJ)

<sup>‡</sup> Hubble, Carnegie-Princeton Fellow

forming galaxies and the underdense IGM with heavy elements (see van de Voort 2017 for a recent review and related references). The presence of heavy elements in turn alters the thermal state of the gas.

Over the last decade, substantial effort has been made to understand the physical mechanisms driving the evolution of the CGM (see Chen 2017a, Tumlinson, Peeples & Werk 2017, for recent reviews), but the origin of the cool  $T\sim 10~{\rm K}^{4-5}$  circumgalactic gas is largely uncertain. In particular, the observed high incidence of chemically enriched cool gas in the vicinities of luminous red galaxies (LRGs; e.g. Gauthier, Chen & Tinker 2009, 2010; Lundgren et al. 2009; Gauthier & Chen 2011; Bowen & Chelouche 2011; Zhu et al. 2014; Huang et al. 2016) remains a puzzle, because LRGs are massive elliptical galaxies at  $z\sim 0.5$  and cool gas is not expected to survive in their host haloes.

By design, the LRGs are selected in the Sloan Digital Sky Survey (SDSS; York et al. 2000) to exhibit colours that resemble nearby elliptical galaxies (Eisenstein et al. 2001). They are characterized by luminosities of  $\gtrsim 3\,L_*$  and stellar masses of  $M_{\rm star}\gtrsim 10^{11}{\rm M}_\odot$  at  $z\approx 0.5$  (e.g. Tojeiro et al. 2011), and exhibit little ongoing or recent star formation (e.g. Roseboom et al. 2006; Gauthier & Chen 2011; Huang et al. 2016). The observed strong clustering amplitude of these galaxies indicates that they reside in haloes of  $M_{\rm halo}\gtrsim 10^{13}\,{\rm M}_\odot$  (e.g. Zheng, Coil & Zehavi 2007; Blake, Collister & Lahav 2008; Padmanabhan et al. 2007). Independent studies have also shown that more than 90 per cent of massive galaxies with  $M_{\rm star}\gtrsim 10^{11}\,{\rm M}_\odot$  in the local universe contain primarily evolved stellar populations (e.g. Peng et al. 2010; Tinker et al. 2013), making LRGs an ideal laboratory for studying the cold gas content in massive quiescent haloes.

Gauthier et al. (2009) noted that the cross-correlation signal of photometrically selected LRGs and Mg II absorbers ( $z \sim 0.5$ ) is comparable to the LRG autocorrelation on scales of  $r_p \lesssim 400$  kpc. The comparable clustering amplitudes on scales of the LRG halo size suggest that a large fraction of the LRGs host an MgII absorber. which is understood to originate in photoionized gas of temperature  $T \sim 10^4$  K (Bergeron & Stasínska 1986; Charlton et al. 2003) and trace high column density clouds of neutral hydrogen column density  $N(\text{H {\sc i}}) \approx 10^{16} - 10^{22} \text{ cm}^{-2}$  (Rao, Turnshek & Nestor 2006). Subsequent spectroscopic studies have indeed uncovered strong Mg II absorbers in a significant fraction of LRG haloes with a mean covering fraction of  $\kappa(Mg II) \gtrsim 15(5)$  per cent at projected distances d < 120 (500) kpc (Gauthier et al. 2010; Huang et al. 2016). In addition, strong Ly  $\alpha$  absorption is commonly found around early-type galaxies at  $\langle z \rangle \approx 0.2$  (Thom et al. 2012; Tumlinson et al. 2013). Furthermore, utilizing multiply lensed quasi-stellar objects (QSOs), Zahedy et al. (2016, 2017a) examined the gas content of the lensing galaxies, which are also massive ellipticals at z = 0.4-0.7, and found that high column density gas exists at projected distances as small as  $\approx 3-15$ kpc from these ellipticals. While absorption-line studies continue to show the presence of chemically enriched cool gas around red galaxies at intermediate redshifts, local 21 cm and CO surveys of elliptical galaxies have also uncovered cold atomic and/or molecular gas in > 30 per cent of nearby ellipticals (e.g. Oosterloo et al. 2010; Serra et al. 2012; Young et al. 2014). Together, these independent studies show that cool gas outlasts star formation in massive quiescent haloes over an extended cosmic time period.

The presence of cool gas in massive haloes challenges theoretical expectations of gaseous haloes from both simple analytic models and numerical simulations. The predominantly old stellar population and quiescent state in these passive galaxies also make it difficult to apply feedback due to starburst and active galactic

nuclei (AGNs) as a general explanation for the presence of these absorbers (e.g. Rahmati et al. 2015; Faucher-Giguère et al. 2016). Applying the large number of SDSS Mg II absorption observations of LRGs at intermediate redshifts to test theoretical predictions requires knowledge of the ionization state and metallicity of the gas, which are not available in most cases. To facilitate direct and quantitative comparisons between observations and theoretical predictions, we are carrying out a systematic study of the CGM around LRGs using the Cosmic Origins Spectrograph (COS) onboard the Hubble Space Telescope (HST). The spectral coverage of COS enables observations of the full H I Lyman series transitions and metal absorption features that probe halo gas under different ionization conditions, including C III  $\lambda$  977, O VI  $\lambda\lambda$  1031, 1037, Si III $\lambda$  1206, and Si II  $\lambda$  1260. The LRGs in our sample are selected based only on their proximity to the sightline of a UV-bright background QSO. No prior knowledge of the halo gas properties was used in the selection. Here we present initial results from our programme.

The paper is organized as follows. In Section 2, we describe the design of the COS-LRG programme and related spectroscopic observations. In Section 3, we present absorption-line measurements. In Section 4, we discuss the general properties found for LRG haloes and their implications. We adopt a standard  $\Lambda$  cosmology,  $\Omega_{\rm M}=0.3$  and  $\Omega_{\Lambda}=0.7$  with a Hubble constant  $H_0=70\,{\rm km\,s^{-1}\,Mpc^{-1}}$  throughout the paper.

#### 2 THE COS-LRG PROGRAMME

To advance a deeper understanding of gas properties in massive quiescent haloes, we are carrying out a COS-LRG program for a systematic study of the CGM around LRGs at intermediate redshifts. The primary goals of the programme are (1) to obtain accurate and precise measurements of neutral hydrogen column density  $N(\mathrm{H\,{\sc i}})$  based on observations of the full hydrogen Lyman series and (2) to constrain the ionization state and chemical enrichment in massive quiescent haloes based on observations of a suite of ionic transitions. The LRGs in our sample are selected without prior knowledge of the presence/absence of any absorption features in the haloes and therefore enable an accurate assessment of the chemical enrichment level in these massive quiescent haloes. Here we describe our program design and associated spectroscopic data for the subsequent absorption-line studies.

#### 2.1 Programme design

To establish a uniform sample of LRGs for a comprehensive study of the ionization state and chemical enrichment in massive quiescent haloes, we cross-correlated UV-bright quasars with FUV \( \leq \) 18.5 mag and all LRGs found at  $z \gtrsim 0.26$  in the literature. We identified spectroscopically confirmed LRGs in the SDSS archive that occur at  $d \le 160$  kpc from the sightline of a UV-bright background quasar to ensure that high-resolution ( $R \equiv \lambda/\Delta \lambda \approx 18\,000$ ) FUV absorption spectra of the QSOs can be obtained using the COS onboard the Hubble Space Telescope for observing and resolving weak ionic absorption features. The maximum projected distance d= 160 kpc corresponds to roughly 1/3 of the virial radius ( $R_{vir}$ ) of a  $10^{13} \,\mathrm{M}_{\odot}$  dark matter halo. It was motivated by the SDSS Mg II survey of Huang et al. (2016), who found a mean covering fraction of >10 per cent at  $d \le 160$  kpc around LRGs for  $W_r(2796) > 0.3$  Å absorbers and >70 per cent for weaker ones with  $W_r(2796) > 0.1$ Å. We limited our search to LRGs at  $z \gtrsim 0.26$  to ensure the ability to constrain neutral hydrogen column density,  $N(H_I)$ , from observations of higher-order Lyman absorption series. In addition, we

Table 1. Summary of the QSO-LRG pair sample.

QSO			LRG									
_		FUV			$\theta$	d						
ID	$z_{\rm QSO}$	(mag)	ID	$z_{\rm LRG}$	(arcsec)	(kpc)	$(u-g)_{\text{rest}}$	$M_{ m r}$	$\log M_{\rm star}/{\rm M}_{\odot}^a$			
SDSSJ 094631.69+512339.9	0.741	18.4	SDSSJ 094632.40+512335.9	0.4076	7.7	41.7	$1.71 \pm 0.12$	$-22.42 \pm 0.06$	11.2			
SDSSJ 140626.60+250921.0	0.867	18.3	SDSSJ 140625.97+250923.2	0.4004	8.8	47.3	$1.77 \pm 0.11$	$-22.36 \pm 0.04$	11.1			
SDSSJ 111132.18+554726.1	0.766	17.5	SDSSJ 111132.33+554712.8	0.4629	13.2	77.1	$1.60 \pm 0.08$	$-23.15 \pm 0.07$	11.4			
SDSSJ 080359.23+433258.3	0.449	18.4	SDSSJ 080357.74+433309.9 <sup>b</sup>	0.2535	19.9	78.5	$1.69 \pm 0.04$	$-22.36 \pm 0.02$	11.1			
SDSSJ 092554.70+400414.1	0.471	18.2	SDSSJ 092554.18+400353.4 <sup>b</sup>	0.2475	21.6	83.7	$1.82 \pm 0.04$	$-22.28 \pm 0.02$	11.1			
SDSSJ 095000.73+483129.2	0.590	17.9	SDSSJ 095000.86+483102.2 <sup>b</sup>	0.2119	27.1	93.7	$1.64 \pm 0.03$	$-22.27 \pm 0.02$	11.0			
SDSSJ 112756.76+115427.1	0.509	18.1	SDSSJ 112755.83+115438.3	0.4237	17.7	98.7	$1.93 \pm 0.16$	$-22.45 \pm 0.06$	11.2			
SDSSJ 124307.57+353907.1	0.547	18.4	SDSSJ 124307.36+353926.3	0.3896	19.3	102.2	$1.90 \pm 0.11$	$-22.81 \pm 0.04$	11.3			
SDSSJ 155048.29+400144.9	0.497	18.1	SDSSJ 155047.70+400122.6 <sup>b</sup>	0.3125	23.3	106.7	$1.54 \pm 0.05$	$-22.51 \pm 0.02$	11.2			
SDSSJ 024651.91-005930.9	0.468	18.0	SDSSJ 024651.20-005914.1	0.4105	19.9	108.6	$1.75 \pm 0.07$	$-23.02 \pm 0.03$	11.4			
SDSSJ 135726.27+043541.4	1.233	19.2	SDSSJ 135727.27+043603.3	0.3296	26.5	125.9	$1.77 \pm 0.07$	$-22.71 \pm 0.03$	11.3			
SDSSJ 091029.75+101413.5	0.463	18.5	SDSSJ 091027.70+101357.2 <sup>b</sup>	0.2641	34.4	140.1	$1.77 \pm 0.04$	$-22.69 \pm 0.02$	11.2			
SDSSJ 141309.14+092011.2	0.460	17.5	SDSSJ 141307.39+091956.7	0.3584	29.8	149.2	$1.70 \pm 0.05$	$-23.83 \pm 0.02$	11.7			
SDSSJ 155304.92+354828.6	0.721	17.7	SDSSJ 155304.32+354853.9	0.4736	26.3	155.9	$1.54 \pm 0.11$	$-22.15 \pm 0.11$	11.0			
SDSSJ 125901.67+413055.8	0.745	18.4	SDSSJ 125859.98+413128.2	0.2790	37.6	159.1	$1.71 \pm 0.03$	$-23.49 \pm 0.02$	11.6			
SDSSJ 124410.82+172104.6	1.282	18.4	SDSSJ 124409.17+172111.9	0.5591	24.8	160.1	$1.73 \pm 0.06$	$-23.35 \pm 0.09$	11.5			

*Notes.*  $^{a}$ Uncertainties in  $M_{star}$  are known to be better than 0.2 dex (e.g. Conroy 2013).

restricted our search to LRGs that occur at a line-of-sight velocity difference of  $\Delta v < -10\,000$  km s<sup>-1</sup> from the background QSO, to avoid confusion with outflowing gas from the quasar (e.g. Wild et al. 2008).

This exercise yielded a unique sample of 16 LRGs with a UVbright background QSO found at  $d \lesssim 160$  kpc. Because both UVbright QSOs and LRGs are rare, the number of projected LRG-QSO pairs with close separations is small. This modest sample size underscores the challenge of probing the CGM in massive quiescent haloes using absorption-line techniques. A summary of the LRG-QSO pair sample is presented in Table 1, which lists for each pair the QSO ID, redshift  $(z_{OSO})$ , and FUV magnitude observed by GALEX in the first three columns, and the LRG ID, redshift ( $z_{LRG}$ ), angular distance ( $\theta$ ) and the corresponding physical projected distance (d) to the QSO sightline, the rest-frame u-gcolour, rest-frame r-band magnitude  $(M_r)$ , and total stellar mass  $(M_{\rm star})$  in the following seven columns. For each LRG, the restframe u - g colour and  $M_r$  were estimated by interpolating between available optical broad-band photometry in the observed SDSS u, g, r, i, and z bandpasses, and  $M_{\text{star}}$  was estimated using the Kcorrect code (Blanton & Roweis 2007) for a Chabrier initial mass function (Chabrier 2003). Error bars in u - g and  $M_r$  reflect 1- $\sigma$  uncertainties in the photometric measurements. Uncertainties in  $M_{\rm star}$  are understood to be dominated by systematic differences in the model priors and are known to be less than 0.2 dex (e.g. Conroy 2013; Moustakas et al. 2013).

Five of the LRGs in our sample overlap with the COS-Halos red galaxy subsample (e.g. Tumlinson et al. 2011; Thom et al. 2012). Comparisons of our COS-LRG sample with the red galaxies studied by the COS-Halos team (e.g. Thom et al. 2012) are presented in Fig. 1, which displays the  $M_{\rm star}$  versus d distribution in the top panel and the  $M_{\rm star}$  versus z distribution in the bottom panel. Note that we have recalculated  $M_{\rm star}$  for all COS-Halos galaxies based on available SDSS photometric measurements. Our estimates of  $M_{\rm star}$  using K-correct are found to be systematically lower than those reported in Werk et al. (2012) by 0.2 dex. The discrepancy can be attributed to the different stellar initial mass functions adopted by these authors. For consistency, we adopt our  $M_{\rm star}$  estimates for all COS-Halos

galaxies in comparisons with the COS-LRG sample. In addition, one galaxy in the COS-Halos red galaxy sample (J1617+0638\_253\_39) satisfies our mass-selected criterion but is not included in the COS-LRG sample. This red galaxy occurs at d = 101 kpc from the background QSO sightline and has  $M_{\rm star} \approx 2 \times 10^{11} \,{\rm M}_{\odot}$ , but the redshift is too low so the Lyman series transitions are not covered by the available COS spectra. While Ly  $\alpha$  is not detected with a  $2-\sigma$  upper limit to the rest-frame absorption equivalent width of  $W_{\rm r}(1215) = 0.14$  Å (Thom et al. 2012), we exclude this from the COS-LRG in order not to bias subsequent analysis on the incidence of cool gas in these massive haloes. We also note that one of the COS-Halos red galaxies, J1133+032\_110\_5 at z = 0.237 and d =18 kpc (red diamond with a dotted circle in Fig. 1), has a neighbouring QSO at the same redshift and d = 124 kpc. Quasar host haloes have been shown to exhibit CGM properties that are different from both starburst and passive galaxies (e.g. Prochaska, Lau & Hennawi 2014; Johnson, Chen & Mulchaey 2015a; see also Chen 2017b for relevant discussions).

Fig. 1 demonstrates that the LRGs form a uniform sample of highmass haloes with  $M_{\rm star}$  ranging from to log  $M_{\rm star}/M_{\odot}=11.7$  and a median of  $\langle \log M_{\rm star}/M_{\odot} \rangle_{\rm COS-LRG}=11.2$  over the redshift range from z=0.21 to z=0.55. In contrast, the COS-Halos red galaxy sample includes predominantly lower-mass halos with  $M_{\rm star}$  ranging from log  $M_{\rm star}/M_{\odot}=10.3$  to log  $M_{\rm star}/M_{\odot}=11.3$  and a median of  $\langle \log M_{\rm star}/M_{\odot} \rangle_{\rm COS-HalosRed}=10.8$  over the redshift range from z=0.14 to z=0.27. The COS-LRG sample therefore offers a unique opportunity both for studying the CGM in the most massive individual galaxy haloes and for comparison with less massive but still quiescent systems.

#### 2.2 COS UV spectroscopy

High-resolution FUV absorption spectra of the background QSOs are available either from our own COS program (Program ID = 14145) or in the *HST* COS data archive. COS with the G130M and G160M gratings and different central wavelengths offers a contiguous spectral coverage from  $\lambda \approx 1140$  Å to  $\lambda \approx 1780$  Å, with a spectral resolution of full-width-at-half-maximum (FWHM)  $\approx$ 

<sup>&</sup>lt;sup>b</sup>COS-Halos red galaxies that match our LRG selection criteria; projected distances updated based on our own calculations.

Table 2. Journal of HST COS observations.

QSO	Grating	$t_{\rm exp}$ (s)	PID
SDSSJ 024651.91-005930.9	G130M/G160M	5121/11129	14145
SDSSJ 080359.23+433258.3	G130M/G160M	5207/6110	11598
SDSSJ 091029.75+101413.5	G130M/G160M	4913/8700	11598
SDSSJ 092554.70+400414.1	G130M/G160M	3765/4303	11598
SDSSJ 094631.69+512339.9	G130M/G160M	5655/15166	14145
SDSSJ 095000.73+483129.2	G130M/G160M	2445/2927	11598
	G130M	2488	13033
SDSSJ 111132.18+554726.1	G130M/G160M	8388/8850	12025
SDSSJ 112756.76+115427.1	G130M/G160M	5147/11173	14145
SDSSJ 124307.57+353907.1	G130M/G160M	10446/20286	14145
SDSSJ 124410.82+172104.6	G160M	7172	12466
SDSSJ 125901.67+413055.8	G130M/G160M	8230/14223	13833
SDSSJ 135726.27+043541.4	G130M/G160M	14148/28205	12264
SDSSJ 140626.60+250921.0	G130M/G160M	5195/14184	14145
SDSSJ 141309.14+092011.2	G130M/G160M	4959/8138	13833
SDSSJ 155048.29+400144.9	G130M/G160M	3804/4160	11598
SDSSJ 155304.92+354828.6	G130M/G160M	2114/2837	11598

17 km s<sup>-1</sup>. The spectral coverage of COS enables observations of the full H I Lyman series transitions and metal absorption features that probe halo gas under different ionization conditions. Common metal absorption lines observable by COS include C  $_{\rm III}$  λ 977, O  $_{\rm VI}$  λλ 1031, 1037, Si  $_{\rm III}$  λ 1206, and Si  $_{\rm II}$  λ 1260. A summary of the COS observations is presented in Table 2, which lists for each QSO the grating used for the spectra, the total exposure time per grating in seconds, and the program ID (PID) under which the data were obtained. Table 2 shows that all but one of the 16 QSOs have both G130M and G160M spectra available. Although only G160M spectra are available in the *HST* archive for SDSSJ 124410.82+172104.6, the LRG in this field occurs at sufficiently high redshift ( $z_{\rm LRG}$  = 0.5591) that the G160M alone already provides the full coverage for its associated Lyman series transitions.

For each QSO, individual one-dimensional spectra produced by the CALCOS pipeline were retrieved from the HST archive, and further processed using our own software. The wavelength calibration for COS spectra has been shown to contain wavelength-dependent errors up to  $\approx 15~\rm km~s^{-1}$  (e.g. Johnson, Chen & Mulchaey 2013; Liang & Chen 2014; Wakker et al. 2015), leading to apparent misalignments of spectral features between different exposures. Additional wavelength calibration effort is therefore needed both to optimize the signal to noise (S/N) in the final combined spectrum and to ensure the accuracy in measuring the kinematic properties of different absorption features.

We developed our own software to perform this necessary wavelength calibration in two steps. First, we corrected the relative wavelength offsets between individual spectra using a low-order polynomial that best describes the offsets between common absorption lines found in different exposures. The common absorption lines include both intervening absorbers at z > 0 and strong Milky Way features, such as Si III λ 1206 and C II λ 1334 in the G130M data and Si II  $\lambda$  1526 and Al II  $\lambda$  1670 in the G160M data. Individual wavelength-corrected spectra were then coadded to form a final combined spectrum. Next, an absolute wavelength correction was performed using a low-order polynomial by registering unsaturated low-ionization Milky Way features to their known wavelengths in vacuum. In general, the absolute wavelength calibration for the G160M spectra was more challenging than that for the G130M data due to the fact that fewer unsaturated lines were available. The final solution was evaluated and verified using available Lyman series of strong intervening H<sub>I</sub> absorbers across the full spectral range. In some cases, a new solution for the G160M spectrum was obtained using only a constant wavelength offset that was determined based on absorption features in the overlapping window between the G130M and the G160M data. When comparing the velocity centroids between low-ionization lines observed in COS and those of Mg II  $\lambda\lambda$  2796, 2803 lines observed in ground-based echelle spectra (FWHM  $\approx 10\, \rm km\ s^{-1}$ ; see the discussion in Section 2.3), we found that the final wavelength solution generated from our software is accurate to within  $\pm 3\, \rm km\ s^{-1}$ . Finally, each combined spectrum was continuum normalized using a low-order polynomial fit to spectral regions free of strong absorption features. The final continuum-normalized spectra have a median  $S/N\approx 10-30$  per resolution element.

#### 2.3 Optical echelle spectroscopy

Optical echelle spectra of the background QSOs are available for 11 of the 16 QSOs in the COS-LRG sample. These echelle spectra extend the wavelength coverage of absorption spectroscopy from  $\lambda \gtrsim 3300$  Å to  $\lambda \gtrsim 5000$  Å, providing additional constraints based on observations of the Fe II absorption series, the Mg II λλ 2796, 2803 doublet features, and Mg 1\(\lambda\) 2852 absorption. Specifically, optical echelle spectra of SDSSJ 024651.91-005930.9, SDSSJ 112756.76+115427.1. SDSSJ 124410.82+172104.6, SDSSJ 135726.27+043541.4, and SDSSJ 140626.60+250921.0 were obtained using the MIKE echelle spectrograph (Bernstein et al. 2003) on the Magellan Clay telescope. The observations were carried out in three separate runs in 2016 September, 2017 January, and 2017 April. We used a 1 arcsec slit and 2 × 2 binning during readout, resulting in a spectral resolution of FWHM  $\approx 11 \, \text{km s}^{-1}$  at wavelength  $\lambda < 5000 \, \text{Å}$ . The echelle data were processed and extracted using a custom software described in Chen et al. (2014) and in Zahedy et al. (2016). Wavelengths were calibrated using a ThAr frame obtained immediately after each science exposure and subsequently corrected to vacuum and heliocentric wavelengths. Relative flux calibrations were performed using a sensitivity function determined from a spectrophotometric standard star observed on the same night as the QSOs. Individual flux-calibrated echelle orders from different exposures were then coadded and combined to form a single final spectrum that covers a wavelength range from  $\lambda \approx 3300$  Å to  $\lambda \approx 9500$  Å for each QSO. Finally, the combined spectrum was continuum normalized using a low-order polynomial fit to the spectral regions free of strong absorption features.

SDSSJ 080359.23+433258.3, Optical echelle spectra of SDSSJ 091029.75+101413.5, SDSSJ 092554.70+400414.1, SDSSJ 095000.73+483129.2, SDSSJ 155048.29+400144.9, and SDSSJ155304.92+354828.6 obtained using HIRES (Vogt et al. 1994) on the Keck Telescopes are available in the Keck Observatory Archive (KOA). The spectra were obtained using a 0.86 arcsec slit and  $2 \times 1$  binning during readout, resulting in a spectral resolution of FWHM  $\approx 6.3 \, \text{km s}^{-1}$ at wavelength  $\lambda < 5900 \, \text{Å}$ . Individual pipeline-reduced echelle orders were retrieved from the KOA, and coadded using our own software to form a single combined echelle spectrum, covering a wavelength range from  $\lambda \approx 3100 \text{ Å to } \lambda \approx$ 5900 Å for each QSO. The combined spectrum was continuum normalized using a low-order polynomial fit to the spectral regions free of strong absorption features. A summary of the available optical echelle spectra is presented in Table 3, which lists for each QSO the echelle spectrograph used, the total accumulated exposure time, and the mean S/N per resolution element at  $\lambda < 5000 \, \text{Å}.$ 

Table 3. Journal of optical echelle observations.

QSO	Instrument	$t_{\rm exp}$ (s)	S/N
SDSSJ 024651.91-005930.9	MIKE	3000	41
SDSSJ 080359.23+433258.3	HIRES	6000	24
SDSSJ 091029.75+101413.5	HIRES	2400	15
SDSSJ 092554.70+400414.1	HIRES	2400	16
SDSSJ 095000.73+483129.2	HIRES	2400	30
SDSSJ 112756.76+115427.1	MIKE	7620	17
SDSSJ 124410.82+172104.6	MIKE	4200	33
SDSSJ 135726.27+043541.4	MIKE	5400	25
SDSSJ 140626.60+250921.0	MIKE	1800	10
SDSSJ 155048.29+400144.9	HIRES	2400	31
SDSSJ 155304.92+354828.6	HIRES	2400	36

## 3 ABSORPTION PROPERTIES IN LRG HALOES

The continuum-normalized UV and optical QSO spectra described in Section 2 provide sensitive constraints for the properties of absorbing gas in massive quiescent haloes. For each LRG halo, we search for corresponding absorption features in the spectrum of the background QSO over a line-of-sight velocity interval of  $\pm 500\,\mathrm{km}$  s<sup>-1</sup> from the systemic redshift of the LRG. This search window corresponds to  $\approx \pm 3\,\sigma_v$ , where  $\sigma_v$  is the observed line-of-sight velocity dispersion of Mg II absorbing gas in LRG haloes (e.g. Huang et al. 2016). It is therefore sufficiently large to include absorption features physically connected to the LRGs.

To characterize the gas content in LRG haloes, we obtain two sets of measurements. First, we perform a Voigt profile analysis, taking into account the presence of multiple absorption components per halo, and determine  $N(\mathrm{H\,{\sc i}})$  and the Doppler parameter  $b_{\mathrm{H\,{\sc i}}}$  of individual components, and the associated measurement uncertainties. Next, we measure the total integrated absorption equivalent widths of different ionic absorption transitions, which enable direct comparisons between absorption properties of the LRG haloes in our study and those of quiescent haloes studied previously (e.g. Gauthier & Chen 2011; Thom et al. 2012; Werk et al. 2013; Huang et al. 2016). Here we describe the absorption line analysis for measuring  $N(\mathrm{H\,{\sc i}})$  and for constraining the incidence of heavy ions in massive quiescent haloes.

### 3.1 $_{HI}$ Measurements of N(HI) and b

The COS-LRG sample is established based on the criterion that robust constraints for  $N({\rm H\,{\sc i}})$  can be placed based on observations of the Lyman series lines. Specifically, observations of the flux decrement at the Lyman limit transition provide a direct constraint for  $N({\rm H\,{\sc i}})$ , while observations of the Lyman absorption lines constrain the Doppler parameter  $b_{\rm H\,{\sc i}}$ . In Figs 2(a) and (b), we present the continuum-normalized final spectra of the LRG halos over the rest-frame spectral range from  $\lambda\lesssim 910~{\rm \AA}$  to Ly  $\gamma$ , organized with increasing projected distance from top to bottom.

For all but two sightlines (SDSSJ 080359.23+433258.3 and SDSSJ 092554.70+400414.1), the available COS data provide a complete spectral coverage for the Lyman series transitions from Ly  $\alpha$  to below Lyman limit. For SDSSJ 080359.23+433258.3, the

<sup>1</sup>The LRG toward SDSSJ 124409.17+172111.9 is found at z = 0.5591 and the corresponding Ly α transition occurs at  $\lambda = 1895$  Å. Therefore, only Ly β and higher Lyman series lines are observed in the COS FUV channel.

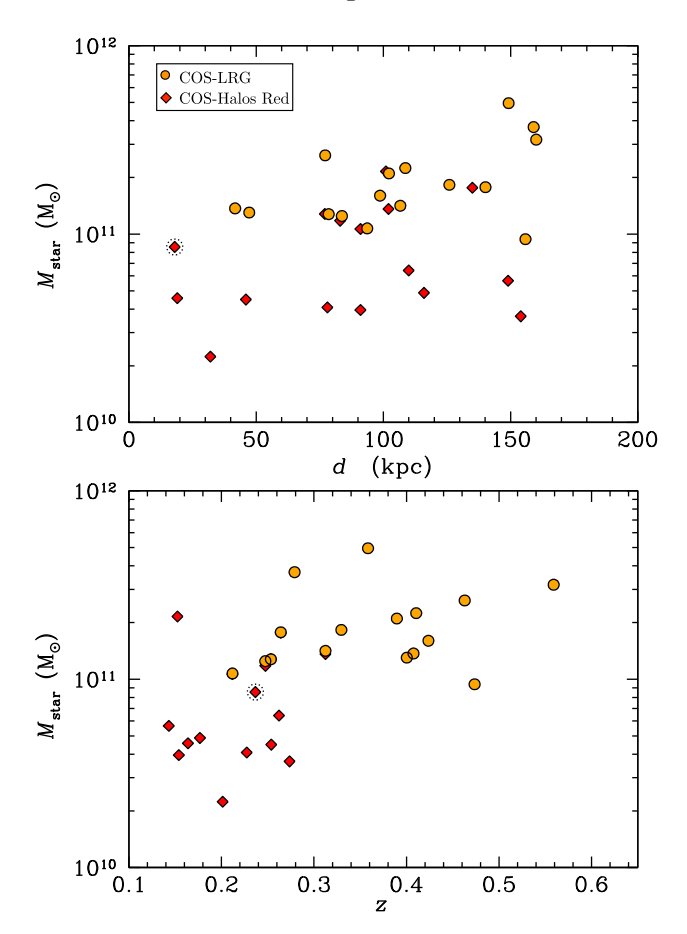


**Figure 1.** Comparisons of the LRGs in our studies (orange filled circles) and the red galaxies in the COS-Halos sample (red diamonds) considered by Thom et al. (2012). The LRGs form a unique, mass-limited sample of quiescent galaxies located at  $d \lesssim 160$  kpc from a UV-bright background QSO.  $M_{\rm star}$  of the LRGs ranges from  $\log M_{\rm star} = 11$  to  $\log M_{\rm star} / M_{\odot} = 11.7$  with a median of  $\langle M_{\rm star} / M_{\odot} \rangle_{\rm COS-LRG} = 11.2$ . In contrast, the COS-Halos red galaxies span a wide range in  $M_{\rm star}$  from  $\log M_{\rm star} / M_{\odot} = 10.3$  to  $\log M_{\rm star} / M_{\odot} = 11.3$  with a median of  $\langle M_{\rm star} / M_{\odot} \rangle_{\rm COS-HalosRed} = 10.8$ . Note that one of the COS-Halos red galaxies, J1133+032\_110\_5 at z = 0.237 and d = 18 kpc (red diamond with a dotted circle), has a neighbouring QSO at the same redshift and d = 124 kpc. Five of the remaining COS-Halos red galaxies satisfy the LRG selection criteria, and are therefore included in the LRG sample. These are shown in both sets of symbols. We have recalculated both  $M_{\rm star}$  and d ourselves for consistency, which led to small offsets in d.

LRG is at z=0.2535 and the available COS spectra do not provide spectral coverage below  $\lambda\approx 930$  Å at the rest frame of the LRG. However, because the absorbing gas along the QSO sightline in this LRG halo is optically thin, observations of Ly  $\alpha$ , Ly  $\beta$ , Ly  $\gamma$ , and Ly  $\delta$  are sufficient for constraining the  $N({\rm H\,{\sc i}})$  without additional higher-order Lyman series lines. For SDSSJ 092554.70+400414.1, the LRG occurs at z=0.2475 and therefore the available COS spectra also do not cover the Lyman limit and higher-order Lyman series lines. However, because the cool gas uncovered along the QSO sightline contains a large neutral gas column and the Ly  $\alpha$  absorption line exhibits prominent damping wings, an accurate measurement of  $N({\rm H\,{\sc i}})$  can also be obtained based on the damped profiles.

For each LRG halo, we perform a Voigt profile analysis using a custom software. We first generate a model absorption spectrum, including the full Lyman series and continuum absorption beyond the Lyman limit, based on the minimum number of discrete com-

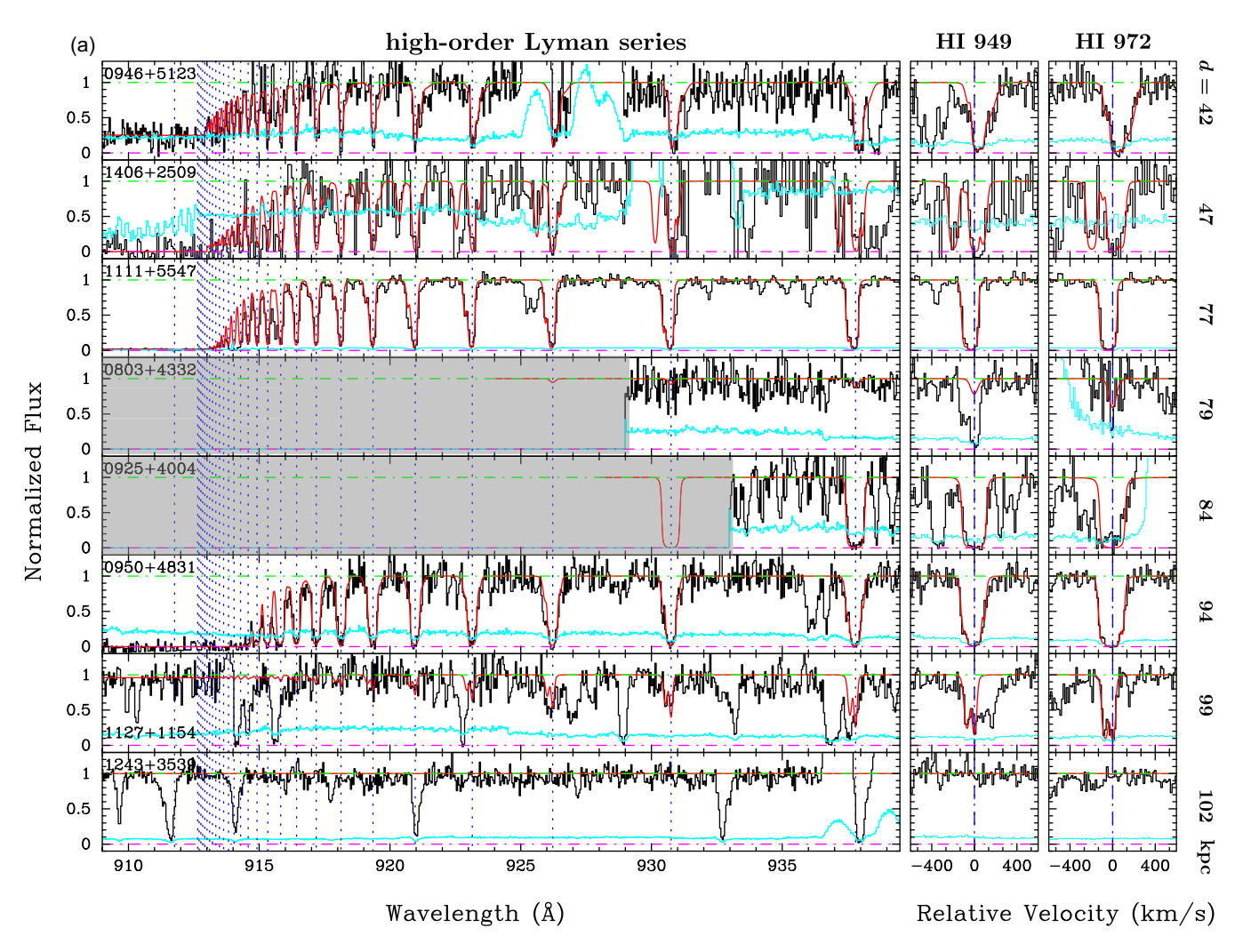


Figure 2. (a) The Lyman series absorption spectra observed at different projected distances from LRGs, from d=42 kpc at the top and increasing to d=102 kpc at the bottom. The continuum-normalized spectra are shown in black with the corresponding  $1-\sigma$  error shown in cyan. The green and red dash-dotted lines mark the normalized continuum and zero flux levels for guidance. For each LRG halo, the velocity profiles of Ly  $\gamma$  and Ly  $\delta$  are presented in the two right panels with zero velocity corresponding to  $z_{abs}$  in Table 4, and the remaining higher-order Lyman series lines, along with the Lyman limit, are presented in the left panel with the blue dotted lines indicating the expected positions of the Lyman transitions. Spectral regions that are not covered by available COS spectra are greyed out. The best-fitting Lyman series absorption spectra are shown in red. (b) Same as part (a), but for LRG haloes at projected distances from d=107 kpc at the top and increasing to d=160 kpc at the bottom. Note that for SDSSJ 155048.29+400144.9 in the top panel the best-fitting  $N(H_1)$  successfully reproduces the full Lyman series lines but predicts a larger flux decrement below the Lyman limit than what is observed in the data by more than 1- $\sigma$ . The acquisition image of the COS observations reveals a second point source in the COS aperture at  $\approx 0.55$  arcsec along the dispersion direction from the QSO, which may have contributed to the excess flux below the Lyman limit of the LRG.

ponents needed to explain the observed absorption profiles. Each component is uniquely defined by three parameters:  $N(H_I)$ ,  $b_{H_I}$ , and the velocity centroid  $dv_c$  relative to the redshift of the strongest absorbing component  $z_{abs}$ . The theoretical Lyman series spectrum is then convolved with the COS line spread function, appropriate for the lifetime position the spectra were obtained at, and binned to the adopted pixel resolution of the data. Next, the model spectrum is compared to the continuum-normalized COS spectrum, and the best-fitting model is found using a  $\chi^2$  minimization routine. Finally, we perform a Markov Chain Monte Carlo (MCMC) analysis using the EMCEE package (Foreman-Mackey et al. 2013), in order to assess the probability distribution of the best-fitting model parameters. The MCMC run consists of 200 steps with an ensemble of 250 walkers, which are initialized over a small region in the parameter space around the minimum  $\chi^2$  value. The MCMC analysis allows us to construct the marginalized probability distribution for each

parameter of the model. The sum of the best-fitting Voigt profiles of individual components is displayed in red solid line for each LRG halo in Figs 2(a) and (b). The best-fitting  $N({\rm H\,I})$  and  $b_{{\rm H\,I}}$  of each component and the corresponding 68 per cent confidence intervals are presented in columns (8) and (9) of Table 4, along with  $z_{\rm abs}$ , relative velocity  $v_{\rm gas-gal}$  of  $z_{\rm abs}$  to  $z_{\rm LRG}$ ,  $dv_{\rm c}$ , and the total  $N({\rm H\,I})$  summed over all components in columns (4) through (8). Note that while the search window in the line-of-sight velocity is large,  $\pm 500\,{\rm km~s^{-1}}$ , all the identified absorption features fall well within this search window with a mean and dispersion between the strongest H I component and the LRG of  $\langle v_{\rm gas-gal} \rangle = 29\,{\rm km~s^{-1}}$  and  $\sigma_{\langle v_{\rm gas-gal} \rangle} = 171\,{\rm km~s^{-1}}$ , consistent with the velocity dispersion found between Mg II absorbing gas and LRGs in the larger SDSS LRG sample in Zhu et al. (2014) and in Huang et al. (2016).

Three of the 16 LRGs do not exhibit any corresponding Lyman absorption series in the search window. These are

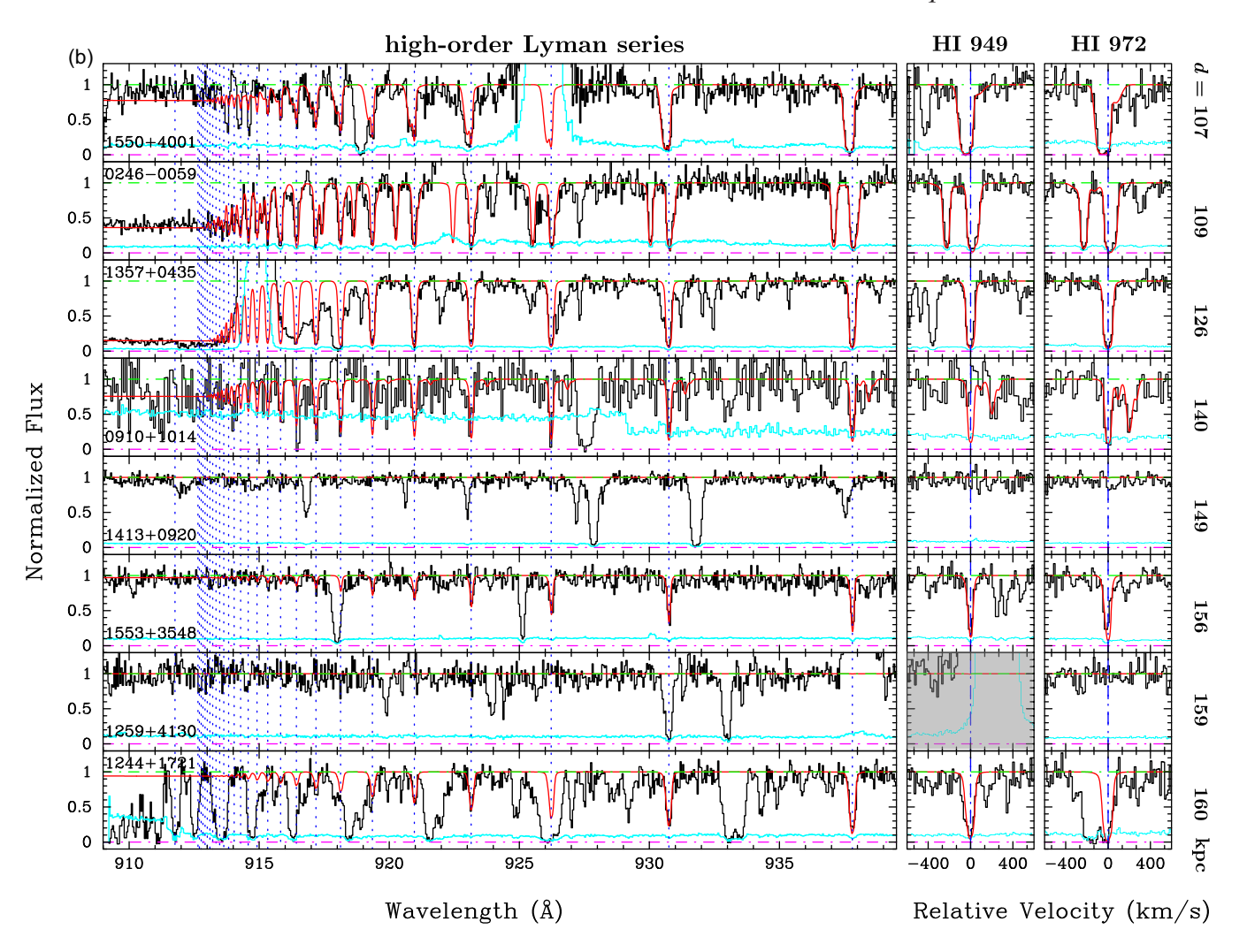


Figure 2 Continued.

SDSSJ 124307.36+353926.3 at z=0.3896 and d=102 kpc, SDSSJ 141307.39+091956.7 at z=0.3584 and d=149 kpc, and SDSSJ 125859.98+413128.2 at z=0.2790 and d=159 kpc. We place a sensitive  $2-\sigma$  upper limit of  $N({\rm H\,{\sc i}})<12.8$  over a wavelength window of  $\pm 16$  km s<sup>-1</sup> around the expected Ly  $\alpha$  location, approximately twice the spectral resolution element of the COS spectra, using the associated 1- $\sigma$  error spectrum for these LRG haloes.

Our analysis shows that high- $N(H_I)$  gas is common in LRG haloes with a median of  $\langle \log N(\text{H {\sc i}}) \rangle_{\text{med}} = 16.6$  at  $d \lesssim 160$  kpc. The spectral coverage of the rest-frame Lyman limit transition proves to be critical for constraining  $N(H_I)$  in these Lyman limit and partial Lyman limit systems. The excellent agreement between the observed and best-fitting absorption profiles of the Lyman series lines and the flux discontinuity at the Lyman limit in Figs 2(a) and (b) demonstrates that our best estimated N(HI) and  $b_{HI}$  in Table 4 are indeed accurate. In one case, SDSSJ 155048.29 + 400144.9 at z=0.3125 and d=107 kpc, we note that the best-fit  $N(\mathrm{H\,{\sc i}})$ successfully reproduces the full Lyman series lines but predicts a larger flux decrement below the Lyman limit than what is observed in the data by more than  $1-\sigma$ . Inspecting the acquisition image of the COS observations, we find a second point source in the COS aperture at  $\approx 0.55$  arcsec along the dispersion direction from the QSO. The excess flux below the Lyman limit of the LRG can be explained if the redshift of this second source is below the redshift of the LRG. We also note a second case, SDSSJ 124409.17+172111.9 at z=0.5591 and d=160 kpc, for which the continuum flux declines to zero below 909 Å in the rest frame of the LRG. An MgII absorber of rest-frame equivalent width  $W_{\rm r}(2796)\approx 0.4$  Å at z=0.5507 toward this QSO sightline has been known and studied extensively by several groups (e.g. Steidel & Sargent 1992; Rao, Turnshek & Briggs 1995; Churchill & Vogt 2001; Zahedy et al. 2017b). This Mg II absorber contains a large neutral gas column of log  $N({\rm H\,I})=19.1\pm0.1$  as revealed in the COS spectra, which explains the flux decrement below 909 Å in the rest frame of the z=0.5591 absorber.

#### 3.2 Absorption equivalent width of heavy ions

In addition to the hydrogen Lyman series absorption features, we also search for associated ionic transitions for constraining the incidence of heavy ions in massive quiescent haloes, including Mg II  $\lambda\lambda$  2796, 2803, Si II  $\lambda$  1260, Si II  $\lambda$  1193, Si III  $\lambda$  1206, C III  $\lambda$  977, and O vI  $\lambda\lambda$  1031, 1037. Figs 3(a) and (b) present the absorption profiles of associated MgII doublet, Si II, Si III, C III, and the O vI doublet transitions found in each LRG halo, along with the hydrogen Ly  $\alpha$  and Ly  $\beta$  absorption lines, both observations and best-fitting Voigt profile models, at the top of each column for comparison. For the three LRGs with no HI absorp-

 Table 4. Summary of LRG halo gas properties.

LRG			Absorption	Properties										
		d		$v_{ m gas-gal}$		$dv_{\rm c}$		$b_{\mathrm{H\tiny I}}$	$W_{\rm r}(1215)$	$W_{\rm r}(977)$	$W_{\rm r}(1031)$	$W_{\rm r}(1206)$	$W_{\rm r}(1260)$	$W_{\rm r}(2796)$
ID	$z_{LRG}$	(kpc)	$z_{abs}$	$(km s^{-1})$	comp.	$({\rm km}\;{\rm s}^{-1})$	$\log N(HI)$	$(km s^{-1})$	(mÅ)	(mÅ)	(mÅ)	(mÅ)	(mÅ)	(mÅ)
(1)	(2)	(3)	(4)	(5)	(6)	(7)	(8)	(9)	(10)	(11)	(12)	(13)	(14)	(15)
SDSSJ 094632.40+512335.9	0.4076	41.7	0.40701	-126	all		$17.34 \pm 0.01$		$1639 \pm 47$	$926 \pm 37$	$800 \pm 27$	$688 \pm 54$	< 420	
				1	$-63.8^{+4.5}_{-4.1}$ $0.0^{+0.4}_{-0.3}$	$14.69^{+0.09}_{-0.08}$	$27.5^{+3.8}_{-3.6}$							
					2	$0.0^{+0.4}_{-0.3}$	$17.32 \pm 0.01$	$12.3^{+0.8}_{-0.7}$						
					3	$+54.6^{+4.0}_{-5.5}$	$16.01^{+0.09}_{-0.10}$	20.0+1./						
					4	$+132.1_{-18.6}^{-130.7}$	$15.41^{+0.14}_{-0.09}$	$29.9_{-3.4}^{+0.8}$ $71.4_{-6.0}^{+9.8}$						
SDSSJ 140625.97+250923.2	0.4004	47.3	0.40040	0	all		$16.01^{+0.09}_{-0.10} \\ 15.41^{+0.14}_{-0.09} \\ 18.04^{+0.14}_{-0.04}$		$1535 \pm 40$	$610 \pm 140$		$433 \pm 30$	$192 \pm 39$	$431 \pm 67$
					1	$-196.9^{+3.2}_{-3.0}$	$16.15 \pm 0.22$	$28.6_{-1.9}^{+2.4}$ $16.6_{-2.2}^{+2.6}$						
					2	$-93.3_{-4.8}^{+5.6}$	$14.15^{+0.14}_{-0.17}$	$16.6^{+2.6}_{-2.2}$						
					3	$0.0^{+0.1}_{-0.1}$	$18.03^{+0.15}_{-0.04}$ $15.68^{+0.23}_{-0.22}$	$20.2_{-1.2}^{+1.0} 26.8_{-2.4}^{+3.0}$						
					4	$+82.7^{+4.0}_{-5.4}$	$15.68^{+0.23}_{-0.22}$	$26.8^{+3.0}_{-2.4}$						
SDSSJ 111132.33+554712.8	0.4629	77.1	0.46352	+127	all		$17.82 \pm 0.01$		$876 \pm 27$	$401 \pm 5$	$67 \pm 10$	$362 \pm 21$		
				1	$-92.1^{+1.6}_{-1.3}$	$15.73 \pm 0.03$	$20.1^{+1.1}_{-1.0}$							
					2	$-30.4^{+2.5}_{-3.0}$	$16.32^{+0.06}_{-0.08}$	$23.9_{-2.0}^{+1.7}$						
					3	$0.0^{+0.6}_{-0.8}$	$17.80 \pm 0.01$	$14.8^{+0.4}_{-0.3}$						
SDSSJ 080357.74+433309.9	0.2535	78.5	0.25330	-48	1	$0.0^{+0.8}_{-0.8}$ $0.0^{+2.4}_{-3.0}$	$14.77 \pm 0.05$	$42.7_{-2.4}^{-3.8}$	$591 \pm 18$	$175 \pm 23$		< 48	< 68	< 29
SDSSJ 092554.18+400353.4	0.2475	83.7	0.24769	+46	1	$0.0 \pm 1.7$	$19.58 \pm 0.02$	$36.2_{-0.6}^{+0.7}$	$3327 \pm 58$	>474		$565 \pm 19$	$730 \pm 37$	$1129 \pm 24$
SDSSJ 095000.86+483102.2	SDSSJ 095000.86+483102.2 0.2119	93.7	0.21169	-52	all		$18.52^{+0.05}_{-0.10}$		$1353 \pm 27$	$689 \pm 15$	$206 \pm 14$	$500 \pm 28$	$312 \pm 16$	$584 \pm 12$
					1	$-96.9^{+9.5}_{-3.1}$	$15.43^{+0.13}_{-0.05}$	$25.8^{+6.2}_{-2.5}$						
					2	$0.0^{+0.7}_{-0.5}$	$15.43_{-0.05}^{+0.13} \\ 18.52_{-0.10}^{+0.05} \\ 15.06_{-0.07}^{+0.11}$	$24.7_{-1.0}^{+2.5}$ $14.4_{-1.7}^{+3.4}$						
					3	$+95.9^{+2.6}_{-5.0}$	$15.06^{+0.11}_{-0.07}$	$14.4^{+3.4}_{-1.7}$						
SDSSJ 112755.83+115438.3	0.4237	98.7	0.42461	+192	all		$15.81 \pm 0.06$		$680 \pm 31$	$185 \pm 10$	$54 \pm 12$	$90 \pm 33$		$62 \pm 26$
					1	$-64.4^{+4.6}_{-3.6}$	$15.45^{+0.07}_{-0.06}$	$29.0_{-2.5}^{+3.3} \\ 16.9_{-2.3}^{+2.4}$						
					2	$0.0^{+3.5}_{-3.4}$	$15.56^{+0.07}_{-0.11}$	$16.9^{+2.4}_{-2.3}$						
SDSSJ 124307.36+353926.3	0.3896	102.2	0.3896			0.0	< 12.8	15 <sup>a</sup>	< 19	< 12	< 8	< 18	< 34	
SDSSJ 155047.70+400122.6	0.3125	106.7	0.31282	+73	all		$16.61 \pm 0.04$		$1264 \pm 24$	$445 \pm 27$	$72 \pm 23$	$360 \pm 26$	< 105	$196 \pm 11$
					1	$-57.1^{+3.3}_{-3.0}$	$16.21 \pm 0.06$	$39.1^{+1.8}_{-1.7}$				•••		
					2	$0.0 \pm 0.1$	$16.38^{+0.07}_{-0.08}$	$13.1 \pm 1.0$		•••				
					3	$+83.2^{+4.8}_{-7.3}$	$14.58 \pm 0.05$	$54.1_{-4.3}^{+7.1}$						
SDSSJ 024651.20-005914.1	0.4105	108.6	0.41168	+251	all		$17.21 \pm 0.01$		$1573 \pm 34$	$365 \pm 26$	$45 \pm 8$	$144 \pm 42$	$146 \pm 32$	$84 \pm 15$
					1	$-310.6^{+6.5}_{-5.5}$	$13.96 \pm 0.06$	$59.0^{+3.1}_{-2.5}$		•••				
					2	$-229.8^{+0.8}_{-0.7}$	$16.49^{+0.06}_{-0.05}$	$17.4 \pm 0.3$	•••	***				
					3	$-128.5^{+0.7}_{-0.9}$	$14.04 \pm 0.05$	$37.2^{+1.1}_{-1.4}$						
					4	$+0.0^{+0.9}_{-0.8}$	$17.11^{+0.01}_{-0.02}$	$16.6 \pm 0.4$						
					5	$+52.5^{+2.5}_{-2.0}$	$15.62^{+0.07}_{-0.08}$	$24.2^{+0.8}_{-0.9}$		•••				
SDSSJ 135727.27+043603.3	0.3296	125.9	0.32869	-205	1	$0.0 \pm 0.4$	$17.483 \pm 0.002$	$18.3 \pm 0.2$	$686 \pm 34$	< 24	< 22	< 46	< 47	< 54
SDSSJ 091027.70+101357.2	0.2641	140.1	0.26341	-164	all		$16.65^{+0.34}_{-0.24}$		$1198 \pm 38$	$681 \pm 48^{c}$		$214 \pm 60$	$73 \pm 30$	$145 \pm 18$

MNRAS 479, 2547–2563 (2018)

**Table 4** – continued

LRG			Absorption	Properties										
ID (1)	z <sub>LRG</sub> (2)	d (kpc) (3)	$z_{abs}$ (4)	$v_{\text{gas}-\text{gal}} (\text{km s}^{-1})$ (5)	comp. (6)	$       \frac{dv_{c}}{(\text{km s}^{-1})}       (7) $	log N(H I) (8)	bH I (km s <sup>-1</sup> ) (9)	$W_{\rm r}$ (1215) (mÅ) (10)	W <sub>r</sub> (977) (mÅ) (11)	$W_{\rm r}(1031)$ (mÅ) (12)	W <sub>r</sub> (1206) (mÅ) (13)	W <sub>r</sub> (1260) (mÅ) (14)	$W_{\rm r}(2796)$ (mÅ) (15)
					1	$0.0 \pm 0.7$	$16.63^{+0.35}_{-0.25}$	$14.9^{+1.0}_{-1.5}$						
					2	$+91.5^{+2.9}_{-2.8}$	$14.34^{+0.15}_{-0.16}$	$19.2^{+2.6}_{-2.7}$						
					3	$+218.7^{+2.3}_{-2.8}$	$15.11^{+0.09}_{-0.10}$	$40.5^{+2.9}_{-2.1}$						
SDSSJ 141307.39+091956.7	0.3584	149.2	0.3584			0.0	< 12.8	$15^{a}$	< 25	< 9	< 6	< 12	< 17	
SDSSJ 155304.32+354853.9	0.4736	155.9	0.47540	+366	1	$0.0^{+1.1}_{-1.2}$	$15.64 \pm 0.04$	$22.9_{-1.0}^{+1.2}$	$638 \pm 76$	$206 \pm 12$	$75 \pm 25$	< 119		$49 \pm 8$
SDSSJ 125859.98+413128.2	0.2790	159.1	0.2790			0.0	< 12.8	15a1.0	< 15	< 13	< 14	< 14	< 21	
SDSSJ 124409.17+172111.9	0.5591	160.1	0.55851	-113	1	$0.0^{+1.3}_{-1.4}$	$15.98 \pm 0.03$	$30.2^{+1.9}_{-1.7}$	$416^{b}$	$306 \pm 14$				$130 \pm 5$

Notes: The purpose of specifying the b value here is for generating the Voigt profile displayed in Figs 2 and 3 for the non-detections.

<sup>&</sup>lt;sup>b</sup> Ly  $\alpha$  is not covered by the available COS spectrum;  $W_r(1215)$  is inferred from the best-fitting log  $N(H_I)$  and b.

 $<sup>^{\</sup>circ}$ Werk et al. (2013) reported  $W_r(977) = 282 \pm 63$  mÅ for this feature. The discrepancy is likely due to a combination of low S/N and uncertainties in the continuum normalization.

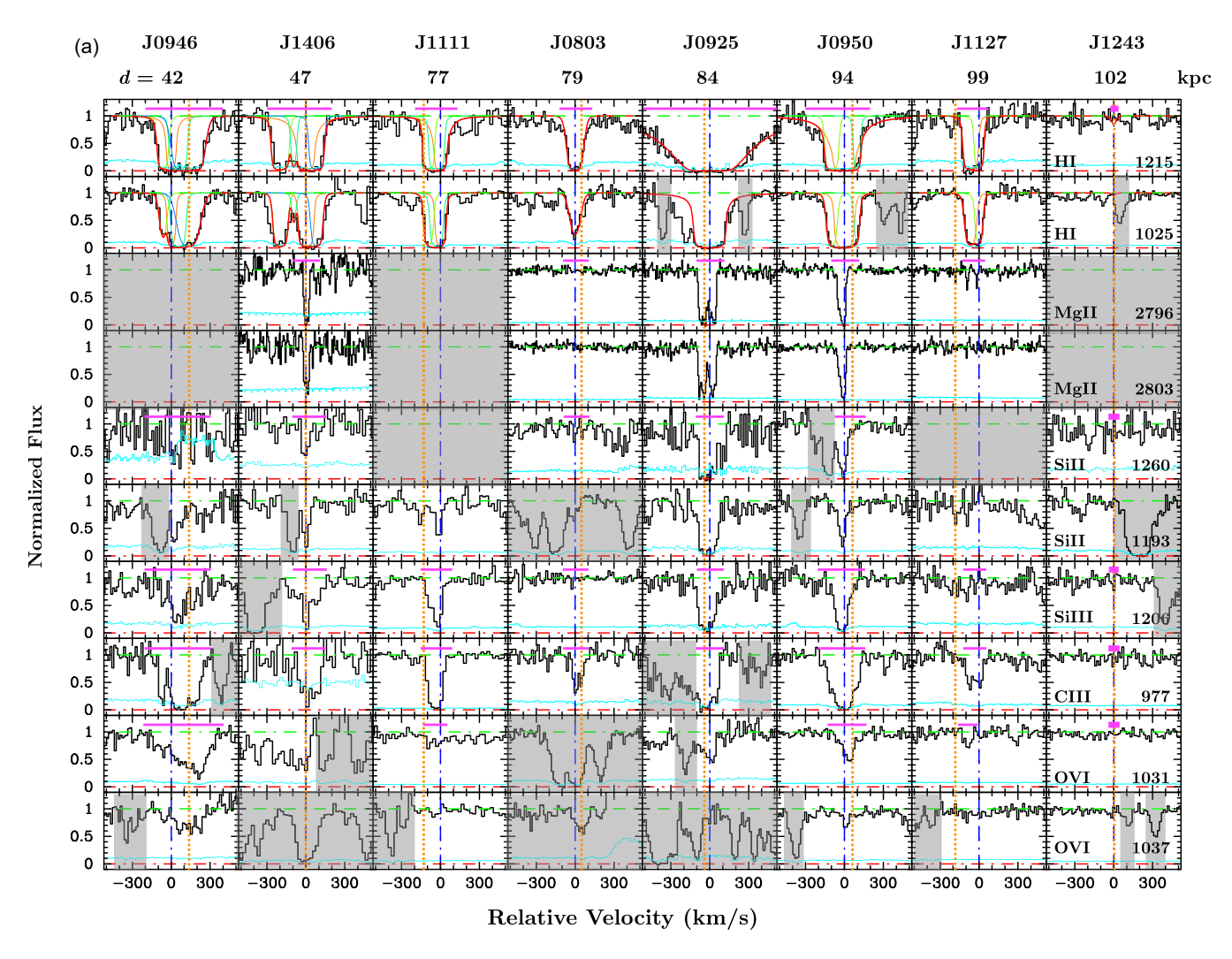


Figure 3. (a) Absorption profiles of (from top to bottom) Ly  $\alpha$ , Ly  $\beta$ , and associated Mgπ, Si π, Si π, CIII, and O vī for eight LRG haloes at d < 105 kpc (increasing d from left to right). Following Fig. 2, zero velocity corresponding to  $z_{abs}$  in Table 4, 1- $\sigma$  errors are shown in cyan. Spectral regions that are either contaminated or not covered by available absorption spectra are greyed out for clarity. Systemic velocities of the LRGs are marked by the vertical dotted line, and the spectral windows used for equivalent width measurements in Table 4 are marked with a horizontal bar at the top of each panel. For the LRG at d = 102 kpc, no absorption features are detected and 2- $\sigma$  upper limits are obtained within ±1 spectral resolution element, the window marked by the thick horizontal bar. For the broad damped Ly  $\alpha$  feature at d = 84 kpc,  $W_r(1215)$  was measured from -800 to 600 km s<sup>-1</sup>. The best-fitting Ly  $\alpha$  and Ly  $\beta$  Voigt profiles, both for individual components separately (thin lines) and for all components combined (thick red line), of each LRG halo are also reproduced in the top two panels for direct comparisons with resolved metal-line components. All LRGs at d < 100 kpc exhibit both hydrogen and associated metal-line absorption features. (b) Same as part (a), but for the remaining eight LRG haloes at d = 107-160kpc. For the LRGs at d = 149 and 159 kpc, no absorption features are detected and 2- $\sigma$  upper limits are obtained within ±1 spectral resolution element, the window marked by the thick horizontal bar. The LRG at d = 126 kpc is the only one of all 13 Ly  $\alpha$  absorbing LRGs in our sample with no detectable metal-line absorption features.

tion detected, we included the Voigt profiles for absorbing gas of  $\log N({\rm H\,{\sc i}})=12.8$  and  $b_{{
m H\,{\sc i}}}=15$  km s<sup>-1</sup> for comparison. Zero velocity corresponds to  $z_{\rm abs}$  in Table 4. For clarity, spectral regions that are not covered by available COS spectra or contain contaminating features are greyed out. For H I, Mg II, Si II, and O VI lines, two transitions are observed which enable identifications of contaminating features based on their known relative line strengths. For Si III and C III, we rely on the matching velocity profiles with other low-ionization lines to identify contaminating features.

We note the excellent agreement in the velocity centroids between individual components of different ionic features, such as the Mg  $\scriptstyle\rm II$  absorption doublets and Si  $\scriptstyle\rm II$ , Si  $\scriptstyle\rm III$ , and C  $\scriptstyle\rm III$ . Recall the issues with COS wavelength calibration described in Section 2.2,

which were corrected using known Milky Way absorption features in our custom data reduction pipeline by forcing the Milky Way lines to their known wavelengths in vacuum. Consequently, an implicit assumption of this process is zero relative motion between the local standard of rest (LSR) and the ISM gas that dominates these absorption features. Such an assumption does not exist in ground-based echelle spectra of Mg II absorption lines, which were calibrated using a combination of comparison lamp and sky lines. The observed excellent agreement between MgII absorption lines and COS observations of Si II, Si III, and C III lines therefore indicates that the relative motion between the Milky Way gas and the LSR toward these sightlines is indeed negligible. In addition, the matching velocity profiles between H I, Mg II, and the remaining

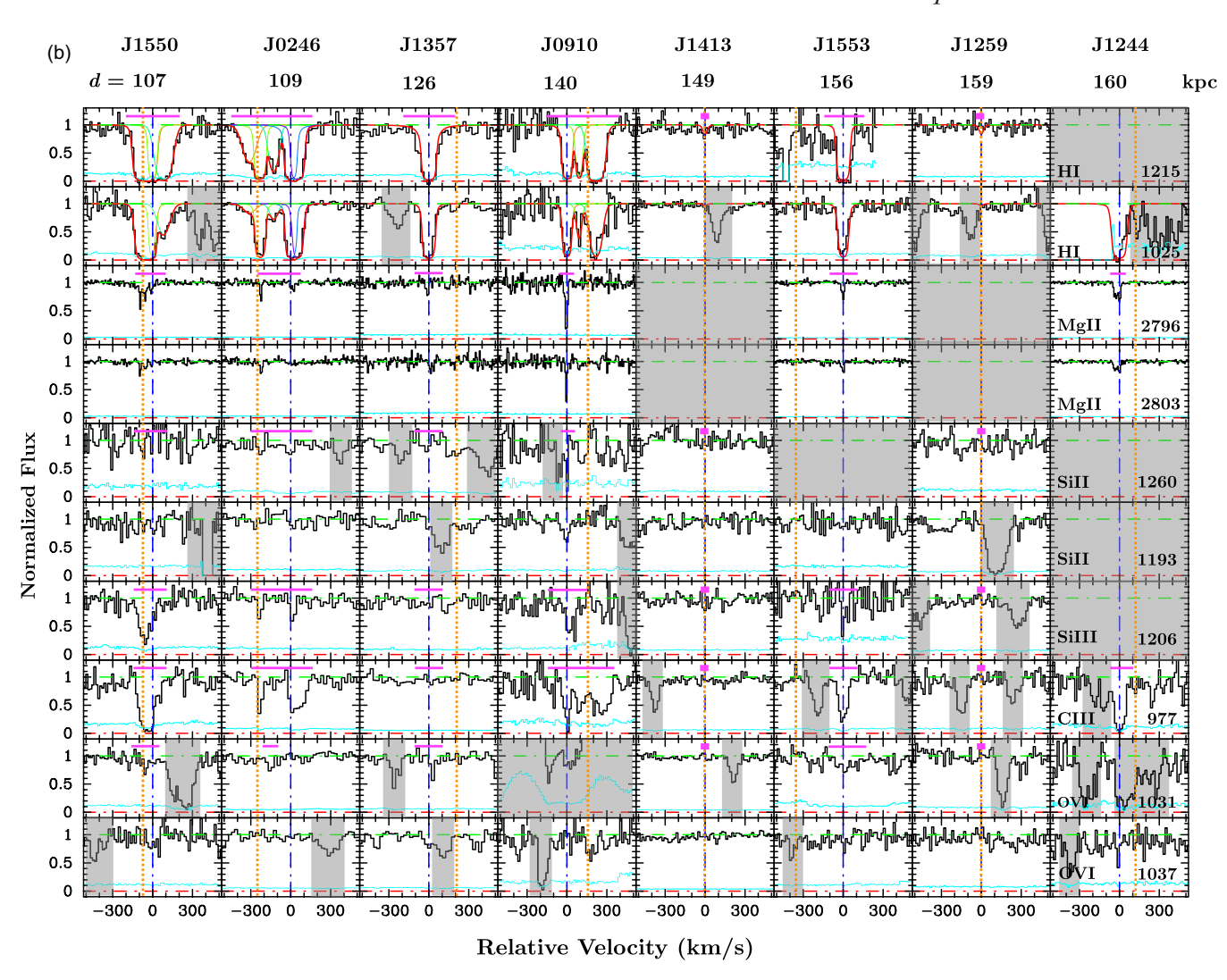


Figure 3 Continued.

FUV lines also provide an important additional guide for filtering out contaminating features.

Two features are immediately clear from Figs 3(a) and (b). First of all, heavy ions are common in these massive quiescent haloes. In all but one LRG with Ly  $\alpha$  and Ly  $\beta$  detected, metal absorption features are also detected (see Section 4.2 for more discussion). Secondly, while the velocity spreads of all the ionic absorption components are seen to extend up to  $\Delta v \approx 200 \text{ km s}^{-1}$  in three cases, e.g. SDSSJ 094632.40+512335.9 at z = 0.4076 and d = 42 kpc, SDSSJ 024651.20-005914.1 at z = 0.4105 and d = 109 kpc, and SDSSJ 091029.75+101413.5 at z = 0.2641 and d = 140 kpc, the line profiles of individual components for all LRG haloes are narrow. The observed narrow component profiles suggest that the gas is photoionized. The only exception is the Ovi doublet transitions detected in the halo of SDSSJ 094632.40+512335.9, which appear broad (FWHM  $\approx 300 \, \text{km s}^{-1}$ ) and asymmetric, indicating a different physical origin from the associated hydrogen and low-ionization gas.

We measure the rest-frame total integrated absorption equivalent widths of both Ly  $\alpha$  and associated ionic lines, including Mg II  $\lambda$  2796, Si III  $\lambda$  1260, Si III  $\lambda$  1206, C III  $\lambda$  977, and O VI  $\lambda$  1031, that are not contaminated by other absorption systems. A local continuum is determined using the line-free spectral region outside

of the designated line features, in order to minimize systematic uncertainties due to continuum placement error. Equivalent width measurement uncertainties are then determined based on the associated 1-sigma error spectrum. For non-detections, we place a  $2-\sigma$ upper limit to the underlying absorption feature over a wavelength window of  $\pm 16 \,\mathrm{km \ s^{-1}}$  around the expected line location, using the associated error spectrum. The wavelength window is chosen to cover approximately twice the spectral resolution element of the COS spectra around the expected lines. The absorption equivalent width measurements and associated uncertainties are presented in columns (9) through (14) of Table 4, along with  $2-\sigma$  upper limits for non-detections. Entries with '...' indicate that either the absorption transitions are not covered by available data or they are blended with contaminating features and therefore no equivalent width measurements are possible. For the five LRGs that have also been studied by the COS-Halos team, equivalent width measurements of these transitions have also been published in Werk et al. (2013). Good agreements, to within  $2-\sigma$  measurement uncertainties, are found in all but one transition. For SDSSJ 091029.75+101413.5 at z = 0.2641 and d=140 kpc, Werk et al. (2013) reported  $W_r=282\pm63$  mÅ for C III  $\lambda$  977, but we measure  $W_{\rm r}(977) = 681 \pm 48$  mÅ. Comparing our continuum-normalized absorption profiles with those presented in fig. 3 of Werk et al. (2013), we find that the discrepancy is likely due to a combination of low S/N and uncertainties in the continuum normalization.

#### 4 DISCUSSION

The absorption-line search described in Section 3 has uncovered strong H<sub>I</sub> absorbers in a large fraction of LRG halos at z =0.21-0.55. Observations of the full hydrogen Lyman series have enabled accurate and precise measurements of N(HI). The median H<sub>I</sub> column density is found to be  $\langle \log N(\text{H}_{\text{I}}) \rangle = 16.6$  at  $d \leq$ 160 kpc (or  $d \lesssim 1/3 R_{\rm vir}$ ) in these LRG haloes. The line-of-sight velocity separations between the HI absorbing gas and LRGs are characterized by a mean and dispersion of  $\langle v_{\text{gas-gal}} \rangle = 29 \text{ km s}^{-1}$ and  $\sigma_{(v_{\rm gas-gal})} = 171 \ {\rm km \ s^{-1}}$ . The observed velocity dispersion of HI gas is similar to what is observed for Mg II absorbing gas (e.g. Zhu et al. 2014; Huang et al. 2016), but less than the expected line-of-sight velocity dispersion for virialized gas in these massive haloes. A suppressed velocity dispersion implies that the kinetic energy of the absorbing clumps is being dissipated, possibly due to the ram-pressure drag force as the clumps move through the hot halo. We refer the readers to Gauthier & Chen (2011) and Huang et al. (2016) for a discussion on the implied mass limit for the clumps.

In addition to accurate  $N({\rm H\,{\sc i}})$  measurements, we have also been able to obtain accurate constraints for  $b_{\rm H\,{\sc i}}$  of individual components. The best-estimated  $b_{\rm H\,{\sc i}}$  values for optically thick components (log  $N({\rm H\,{\sc i}}) > 17.2$ ) are all relatively narrow with  $b_{\rm H\,{\sc i}} \lesssim 20$  km s<sup>-1</sup>, indicating a relatively cool gas temperature of  $T \lesssim 3 \times 10^4$  K. Combining the observed H  $_{\rm I}$  absorption profiles with those of low-, intermediate-, and high-ionization species provides a unique opportunity for constraining the ionization condition, thermal state, and chemical abundances of the CGM in massive quiescent haloes. A detailed ionization analysis is presented in a subsequent paper (Zahedy et al., in preparation). Here we discuss general halo gas properties observed around LRGs.

#### 4.1 Optically thick gas in LRG haloes

Our survey shows not only that H<sub>I</sub> absorbers are frequently seen at d < 160 kpc in LRG haloes, but also that a large fraction (7/16) of these absorbers are optically thick to an ionizing radiation field with log  $N(\rm H_{I}) > 17.2$ , corresponding to an optical depth at the Lyman edge of  $\tau_{\rm 912} > 1$ . Such a high rate of incidence exceeds the expectation from random background counts. We estimate the expected number of random Lyman limit systems (LLSs) in the redshift range surveyed in the COS-LRG sample by adopting the number density of z < 1 LLSs from Ribaudo et al. (2011a) and Shull et al. (2017). Over the search window of  $\pm 500$  km s<sup>-1</sup> around 16 LRGs at  $z \approx 0.4$ , we only expect to find between 0.02 and 0.04 LLSs over the entire COS-LRG sample.

In addition, the observed large clustering amplitude of LRGs (e.g. Padmanabhan et al. 2007; Zheng et al. 2007; Gauthier et al. 2009) also indicates that there are on average more lower-mass galaxies clustered around the LRGs than typical  $L_*$  galaxies on scales of Mpc and, through redshift space distortions, absorbing gas in these correlated haloes could contribute to the detection statistics around LRGs. No clustering measurements are available for LLSs at low redshifts. We therefore infer the contribution from correlated galaxy haloes from observations of MgII in the outskirts of galaxy clusters (Lopez et al. 2008; see also Muzahid et al. 2017). Lopez et al. (2008) reported a factor of 4–9 overabundances in strong MgII absorbers ( $W_r(2796) > 1$  Å) at d < 1 Mpc from galaxy clusters. Taking into account possible enhancement due to clustering leads to a total

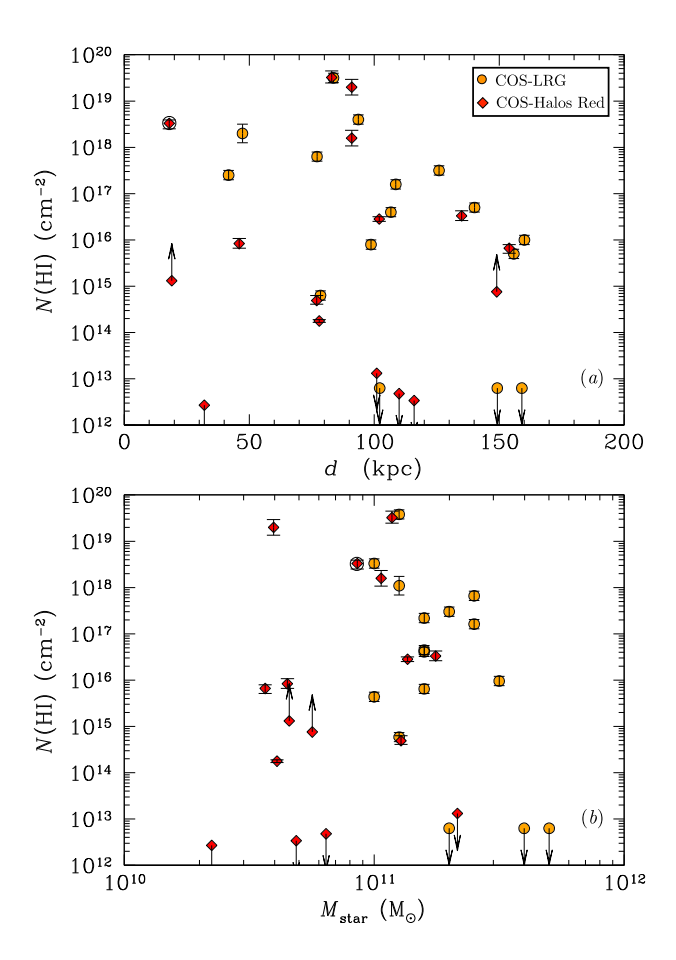


**Figure 4.** *Top*: The observed spatial distribution of N(H1) as a function of projected distance d for the COS-LRG sample (filled circles), in comparison to those found for the COS-Halos red galaxies (red diamonds; Thom et al. 2012). Downward arrows represents a 2-σ upper limit to the underlying N(H1) for haloes with no Ly α absorption line detected. The COS-Halos measurements have been updated based on the report of Prochaska et al. (2017). For two of the COS-Halos red galaxies, the available Lyman series lines are all saturated and therefore only lower limits to N(H1) are available. These are shown as upward arrows. *Bottom*: Distribution of N(H1) versus  $M_{\text{star}}$  for both COS-LRG and COS-Halos red samples. Recall that COS LRGs form a mass-limited sample of log  $M_{\text{star}} \gtrsim 11$  with a median of  $\langle \log M_{\text{star}} / M_{\odot} \rangle_{\text{COS-LRG}} = 11.2$  at z = 0.2-0.55, while the COS-Halos red sample includes predominantly lower-mass galaxies with a median of  $\langle \log M_{\text{star}} / M_{\odot} \rangle_{\text{COS-HalosRed}} = 10.8$  at z = 0.14-0.27. No correlation is found between N(H1) and  $M_{\text{star}}$ .

of between 0.08 and 0.36 expected random and correlated LLSs over the  $\pm 500\,\mathrm{km~s^{-1}}$  velocity window along 16 LRG sightlines. This relatively small number of expected LLSs from random and correlated counts, in contrast to seven LLSs detected at  $d<160\,\mathrm{kpc}$  and  $|v_{\mathrm{gas-gal}}|\lesssim 350\,\mathrm{km~s^{-1}}$  from 16 LRGs, provides a strong support for a physical connection between the observed optically thick gas and the LRGs.

We present the spatial distribution of  $N({\rm H\,{\sc i}})$  as a function of d for the COS-LRG sample in Fig. 4(a). For comparison, we also include the COS-Halos red galaxies (Thom et al. 2012) with updated  $N({\rm H\,{\sc i}})$  from Prochaska et al. (2017). In Fig. 4(b), we show the distribution of  $N({\rm H\,{\sc i}})$  versus  $M_{\rm star}$  for both samples. No correlation is found between  $N({\rm H\,{\sc i}})$  and  $M_{\rm star}$ . Recall that the COS-LRG sample is uniformly defined to have  $\log M_{\rm star}/M_{\odot} \gtrsim 11$  with a median and dispersion of  $\langle \log M_{\rm star}/M_{\odot} \rangle_{\rm COS-LRG} = 11.2$  and  $\sigma_{\langle \log M_{\rm star}/M_{\odot} \rangle_{\rm COS-LRG}} =$ 

0.2 dex at z=0.21-0.55, while the COS-Halos red sample includes a large fraction of lower-mass galaxies with a median and dispersion of  $\langle \log M_{\rm star}/{\rm M}_{\odot} \rangle_{\rm COS-HalosRed}=10.8\pm0.3$  and  $\sigma_{\langle \log M_{\rm star}/{\rm M}_{\odot} \rangle_{\rm COS-HalosRed}}=0.3$  dex at z=0.14-0.27. While there exists a substantial scatter in the observed  $N({\rm H\,I})$ , a large fraction of the COS-LRG and the COS-Halos red samples contain optically thick gas at  $d\lesssim 100$  kpc and a general declining trend of  $N({\rm H\,I})$  is also seen toward larger distances.

We determine the covering fraction and associated uncertainties of optically thick gas in massive quiescent haloes following the maximum-likelihood approach described in Chen et al. (2010). The likelihood of observing an ensemble of LRGs with n showing associated LLSs and m non-detections is given by

$$\mathcal{L}(\kappa_{\text{LLS}}) = \langle \kappa \rangle_{\text{LLS}}^{n} [1 - \langle \kappa \rangle_{\text{LLS}}]^{m}. \tag{1}$$

The full COS-LRG sample probes the LRG haloes out to  $d \approx 160\,\mathrm{kpc}$  (or  $d \approx 1/3\,R_\mathrm{vir}$ ). Based on the detection of LLSs in 7 of the 16 LRG haloes, we estimate a mean covering fraction of optically thick gas of  $\langle\kappa\rangle_\mathrm{LLS}=0.44^{+0.12}_{-0.11}$  at  $d\lesssim 160\,\mathrm{kpc}$ . The error bars represent the 68 per cent confidence interval. In the inner haloes, where we detect LLSs in five of the seven LRG haloes, the mean covering fraction is  $\langle\kappa\rangle_\mathrm{LLS}=0.71^{+0.11}_{-0.20}$  at  $d\lesssim 100\,\mathrm{kpc}$ . We note that excluding five COS-Halos red galaxies does not change the results. We estimate  $\langle\kappa\rangle_\mathrm{LLS}=0.45^{+0.14}_{-0.13}$  at  $d\lesssim 160\,\mathrm{kpc}$  based on five detections of LLS around 11 randomly selected LRGs.

The observed covering fraction of optically thick gas in massive quiescent haloes at  $z \approx 0.4$  is surprisingly consistent with the measurement of  $\langle \kappa \rangle_{\rm LLS} = 0.6^{+0.2}_{-0.1}$  at  $d \lesssim 80$  kpc from  $L_*$  and sub- $L_*$  star-forming galaxies at  $z \approx 0.2$  from the COS-Halos survey (e.g. Prochaska et al. 2017). It is also very comparable to  $\langle \kappa \rangle_{\rm LLS} = 0.64^{+0.07}_{-0.10}$  observed at  $d \lesssim 122$  kpc in quasar host haloes (e.g. Hennawi et al. 2006; Prochaska, Hennawi & Simcoe 2013) and  $\langle \kappa \rangle_{\rm LLS} = 0.30 \pm 0.14$  observed at  $d \lesssim R_{\rm vir}$  in haloes hosting starburst galaxies at  $z \approx 2.3$  (e.g. Rudie et al. 2012). Quasars are typically found to reside in dark matter haloes of mass  $M_{\rm h} \sim 10^{12.5}\,{\rm M}_{\odot}$  (e.g. White et al. 2012), while the targeted starburst galaxies at  $z \approx 2.3$ have a characteristic halo mass of  $M_{\rm h} \sim 10^{12}\,{\rm M}_{\odot}$  (e.g. Adelberger et al. 2005). Both populations reside in lower-mass haloes at z > 2than the LRGs at  $z \approx 0.4$ . To reproduce the observed high gas covering fraction in these distant haloes in cosmological simulations, it is necessary to invoke energetic feedback due to either AGN in quasar host galaxies (e.g. Rahmati et al. 2015) or massive stars (e.g. Faucher-Giguère et al. 2016). The quiescent state of the LRGs makes either AGN or stellar feedback a challenging scenario for explaining the frequent appearance of optically thick gas in these massive haloes.

At the same time, we note the stark contrast between LRG haloes at  $z\approx 0.4$  and the M31 halo. For the M31 halo, the covering fraction of optically thick gas is constrained to be < 5 per cent based on deep 21 cm surveys (Howk et al. 2017), while the covering fraction of Si III absorbing gas is found to approach unity from absorption spectroscopy of background QSOs (Lehner, Howk & Wakker 2015). The lack of optically thick gas coupled with a high covering fraction of heavy ions suggests that either the halo gas is highly ionized or the absorbing clouds are significantly smaller than the beam size ( $\approx 2$  kpc in diameter) of the 21 cm observations (e.g. Rigby, Charlton & Churchill 2002; Stern et al. 2016). M31, with a star formation rate (SFR) of  $\approx 0.4$  M $_{\odot}$  yr $^{-1}$  (e.g. Barmby et al. 2006; Rahmani, Lianou & Barmby 2016), resides in a dark matter halo of  $M_h \approx 10^{12}$  M $_{\odot}$  (e.g. Watkins, Evans & An 2010; Sofue 2015). A lack of optically thick gas would be qualitatively consistent with the observed low

SFR in M31's disc, but different from what is observed for massive quiescent haloes at  $z \approx 0.4$ .

With the observed large covering fraction of optically thick gas in LRG haloes, we proceed to evaluate the fractional contribution of LRGs to the LLS observed along random QSO sightlines. The expected number of LLSs per unit redshift per line of sight originating in LRG haloes is computed following

$$n_{\rm LLS}({\rm LRG}) = \frac{c}{H_0} \frac{(1+z)^2}{\sqrt{\Omega_M (1+z)^3 + \Omega_\Lambda}} \times \int_{L_{\rm min}}^{\infty} dL \, \phi(L) \langle \kappa \rangle_{\rm LLS} (\pi \, R_{\rm gas}^2), \tag{2}$$

where c is the speed of light,  $\phi(L)$  is the LRG luminosity function,  $R_{\rm gas}$  is the radius of gaseous haloes, and  $L_{\rm min}$  is the minimum luminosity of LRGs, which is approximately 3  $L_*$  for the COS-LRG sample, with a corresponding absolute i-band magnitude of  $M_i = -22.6$ . Here we have assumed that the gas cross-section does not vary significantly with luminosity. Adopting the LRG luminosity function of Montero-Dorta et al. (2016), which is characterized by  $M_{i*} = -21.4$  and  $\phi_* = 7.58 \times 10^{-4}$  Mpc<sup>-3</sup>, we find  $n_{\rm LLS}({\rm LRG}) \approx 0.0053$  for  $R_{\rm gas} = 160$  kpc and  $\langle \kappa \rangle_{\rm LLS} = 0.44$ . The observed number density of LLS with log  $N({\rm H\,I}) \geq 17.2$  is  $n_{\rm LLS} = 0.36 - 0.5$  at z < 1 from Ribaudo et al. (2011a) and Shull et al. (2017). We therefore conclude that despite a high covering fraction of optically thick gas in the inner 160 kpc in the radius of massive quiescent haloes, these objects are too rare to contribute more than 2 per cent of the observed LLSs at z < 1 along random OSO sightlines.

#### 4.2 Incidence of heavy ions around LRGs

A primary motivation of the COS-LRG program is to understand the origin and significance of Mg II absorbers found in LRG haloes (e.g. Gauthier et al. 2009, 2010; Bowen & Chelouche 2011; Gauthier & Chen 2011; Huang et al. 2016). The COS-LRG sample is established without prior knowledge of the presence/absence of any absorption features in the haloes, including metal absorption lines. It therefore provides a necessary baseline calibration for characterizing the significance of metal-line absorbers in these massive quiescent haloes. The expanded spectral coverage from combining COS FUV and ground-based echelle spectra also provides empirical constraints for multiple ionization species, from singly ionized silicon and magnesium, to twice-ionized carbon and silicon, and to highly-ionized O<sup>5+</sup>.

Fig. 5 shows the rest-frame absorption equivalent width,  $W_{\rm r}$  versus d for Ly  $\alpha$  and associated metal absorption features, including Mg II  $\lambda$  2796, Si III  $\lambda$  1260, Si III  $\lambda$  1206, C III  $\lambda$  977, and O VI  $\lambda$  1031. For all but one LRG halo with HI absorbers detected, associated metal absorption features are also detected with intermediate ions revealed by C III  $\lambda$  977 and Si III  $\lambda$  1206 being the most dominant ionization state, exceeding both low-ionization gas probed by Mg II and highly ionized gas probed by OvI. For the three LRGs without an HI absorber detected, no metal absorption lines are found to sensitive upper limits.

SDSSJ 135726.27+043541.4 at z=0.3296 and d=126 kpc is the only LRG displaying no trace of metal absorption lines to 2- $\sigma$  limits of < 0.09 Å, while showing a strong Lyman absorption series with log  $N({\rm H\,{\sc i}})=17.5$ . The presence of optically thick gas combined with a complete absence of ionic absorption features places a stringent upper limit of gas metallicity at  $\lesssim 0.3$  per cent solar (see Zahedy et al., in preparation), representing the lowest-metallicity gas detected near a luminous galaxy at intermediate

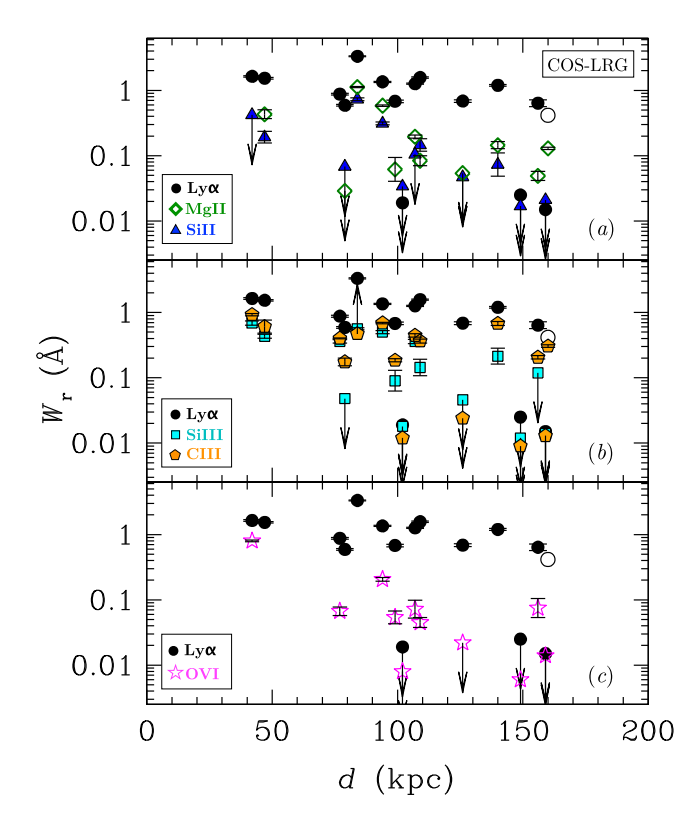


**Figure 5.** Measurements of rest-frame absorption equivalent width,  $W_r$ , versus d for different absorption transitions. Panel (a) presents lowionization Mg II λ 2796 (open diamonds) and Si II λ 1260 (filled triangles) transitions; panel (b) presents intermediate-ionization Si III λ 1206 (filled squares) and C III  $\lambda$  977 (filled pentagons) transitions; and panel (c) presents high-ionization O vi λ 1031 transitions (star symbols). Measurements for Ly  $\alpha$  (black circles) are included in all three panels for comparisons. For SDSSJ 124409.17+172111.9 at z = 0.5591 and d = 160 kpc,  $W_r(1215)$  is shown as an open circle because Ly  $\alpha$  is not covered by the available COS spectrum and  $W_r(1215)$  is inferred from the best-fitting log  $N(H_I)$  and b. For all but one LRG haloes with Ly  $\alpha$  detected, associated metal absorption lines are also detected, with C III λ 977 and Si III λ 1206 being the two most dominant features. The only exception is SDSSJ 135726.27+043541.4 at z = 0.3296 and d = 126 kpc for which optically thick gas is present with  $\log N(\text{H {\sc i}}) = 17.5$  but no metal absorption lines are detected to 2- $\sigma$  limits of < 0.05 Å.

redshift (cf. Ribaudo, Lehner & Howk 2011b; Prochaska et al. 2017). This low metallicity is among the most metal-poor LLSs at z < 1 (e.g. Wotta et al. 2016) and suggests that the absorber originates in inflows of pristine IGM into the LRG halo (e.g. Hafen et al. 2017). The detection of a chemically pristine Lyman limit absorber at z = 0.33 also shows that the intergalactic medium at z < 1 may not be as chemically enriched as previously thought (e.g. Shull, Danforth & Tilton 2014; Lehner 2017).

The presence of heavy ions in all but one COS LRG halo with strong H<sub>I</sub> absorbers indicates widespread chemical enrichment in these massive quiescent haloes. An early result of the COS-Halos survey is the Ovi 'bimodality' in galaxy haloes (Tumlinson et al. 2011): Galaxies with a higher specific SFR exhibit on average stronger Ovi absorption features in their haloes than those with a low specific SFR. This phenomenon is commonly attributed to a causal connection between star formation in galaxies and stellar feedback driven chemical enrichment in galaxy haloes (e.g. Ford et al. 2013; Suresh et al. 2015), in which case the observed heavy elements in galaxy haloes are ejected from galaxies by newly formed young

stars and the origin of heavy elements in quiescent haloes remains unknown. Alternatively, because low specific SFR galaxies in the COS-Halos sample are also more massive than their star-forming counterparts, the deficit of strong Ovi absorption observed in these passive galaxies can also be understood as due to oxygen being ionized to higher ionization states (e.g. Oppenheimer, Crain & Schaye 2016). In this case, the presence/absence of O vi is not directly connected to star formation or AGN feedback, but it requires the CGM to be pre-enriched to  $\geq 1/10$  solar at  $< R_{\rm vir}$ . Adopting an equivalent width threshold of 0.1 Å, we estimate a mean gas covering fraction of  $\langle \kappa(\text{O VI}) \rangle_{0.1} = 0.18^{+0.16}_{-0.06}$ , consistent with the finding for COS-Halos red galaxies (e.g. Werk et al. 2013). While quiescent galaxies exhibit on average fewer strong O vi absorbers of column density  $\log N(O \text{ vi}) > 14 \text{ than star-forming galaxies at } d < 160 \text{ kpc}, \text{ the}$ mean gas covering fraction of moderately strong OVI absorbers of log N(O VI) > 13.5 is found to remain high at  $\approx 50$  per cent in quiescent haloes (Johnson, Chen & Mulchaey 2015b).

Of the 16 galaxies in the COS-LRG sample, 5 do not have constraints for Ovi absorption because the spectral regions are contaminated by either geocoronal emission or other strong features. For the 11 LRGs with available constraints on the O vi absorption strength, 6 have associated Ovi absorbers of  $W_r(1031) > 0.05$  Å, corresponding roughly to log N(O vi) > 13.5 under the linear curve-of-growth assumption. We estimate a mean covering fraction of  $\langle \kappa(O vi) \rangle_{0.05} = 0.55^{+0.13}_{-0.14}$ , extending previous findings to highermass quiescent galaxies.

Similarly, 11 of the 16 QSO–LRG pairs have optical echelle spectra of the QSOs available for constraining the absorption strengths of the associated MgII lines. These high signal-to-noise and high spectral resolution echelle spectra have allowed us both to uncover very weak MgII absorption features of total integrated  $W_r(2796) \gtrsim 0.05$  Å that had been previously missed in SDSS spectra and to resolve individual components (see Fig. 3). While only 3 of the 11 COS LRGs have associated MgII absorbers of  $W_r(2796) > 0.3$  Å, only 2 of these LRGs do not have associated MgII absorption detected to a  $2-\sigma$  upper limit of  $W_r(2796) \approx 50$  mÅ. Fig. 6 presents a comparison of  $W_r(2796)$  versus d between the COS-LRG sample and the SDSS LRG samples, both passive (red symbols) and LINER-like (green), from Huang et al. (2016).

The mean covering fraction of Mg II absorbing gas at  $d \lesssim 160$  kpc is found to be  $\langle \kappa({\rm Mg\,II})\rangle_{0.3}=0.27^{+0.16}_{-0.09}$  for a minimum absorption equivalent width  $W_0 = 0.3$  Å, consistent with the mean covering fraction found using the full SDSS LRG sample from Huang et al. (2016). For a more sensitive limit of  $W_0 = 0.1$  Å, we estimate  $\langle \kappa(\text{Mg II}) \rangle_{0.1} = 0.55^{+0.13}_{-0.14}$  at d < 160 kpc, comparable to what is observed in lower-mass, star-forming galaxies (e.g. Chen et al. 2010; Werk et al. 2013). As a cautionary note, none of the three 'transparent' haloes with no detectable Ly  $\alpha$  have optical echelle spectra available. Consequently, these LRGs do not contribute to the estimates of MgII gas covering fraction here. The estimated mean value above therefore likely represents an upper limit to the true value. Including the three 'transparent' haloes as non-detections in MgII places a lower limit at  $\langle \kappa(Mg II) \rangle_{0,1} > 0.43$ . Combining these limits, we therefore infer a mean covering fraction of MgII absorbing gas in the range of  $\langle \kappa(\text{Mg II}) \rangle_{0.1} \approx 0.4 - 0.55$  in LRG haloes.

A surprising finding of the COS-LRG survey is the significantly higher incidence of C III than Mg II absorption features around LRGs, indicating that chemically enriched cool gas is more abundant in these massive quiescent haloes than previously thought from searches of associated MgII absorption. Twelve of the 16 LRGs in the sample exhibit associated C III with  $W_r(977) > 0.1$  Å, leading to a mean covering fraction of  $\langle \kappa(C \, \text{III}) \rangle_{0.1} = 0.75^{+0.08}_{-0.13}$  for a min-

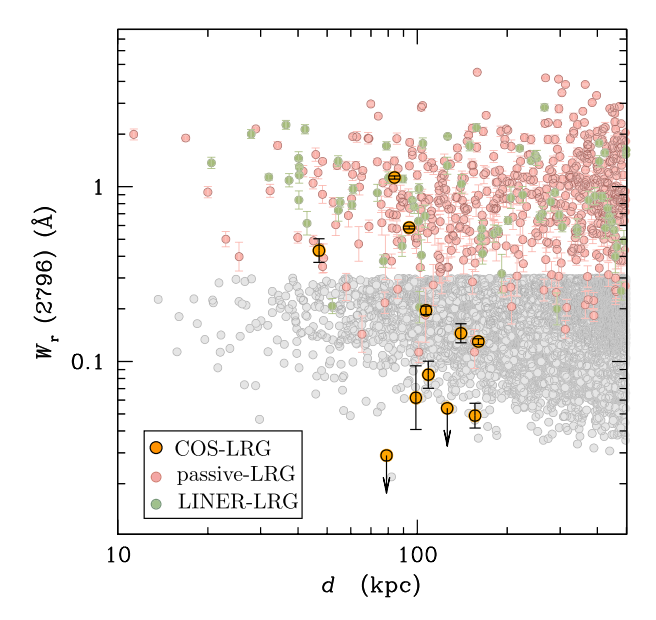


**Figure 6.** Comparison of rest-frame absorption equivalent width,  $W_r(2796)$ , versus d for 11 COS LRGs (orange circles) with ground-based echelle absorption spectra available and the SDSS LRG samples from Huang et al. (2016). Recall that roughly 10 per cent of LRGs exhibit LINER features (e.g. Johnston et al. 2008; Hodge et al. 2008). These LINER-like galaxies are shown in green circles, while the remaining 90 per cent of passive LRGs are shown in red. Available echelle spectra for the COS LRGs have allowed us to uncover very weak Mg II absorption features of total integrated  $W_r(2796) \gtrsim 0.05$  Å that have been previously missed in SDSS spectra. While only 3 of the 11 COS LRGs have associated MgII absorption were detected to a 2- $\sigma$  upper limit of  $W_r(2796) \approx 50$  mÅ.

imum rest-frame absorption equivalent width of  $W_0 = 0.1$  Å at  $d \lesssim 160$  kpc. The observed high covering fraction of C III absorbing gas in LRG haloes is comparable with what is reported for COS-Halos red galaxies with  $\langle \kappa(\text{C III})_{\text{COS-Halosred}} \rangle_{0.1} = 0.79^{+0.11}_{-0.31}$  by Werk et al. (2013), which is also statistically consistent with what is seen in COS-Halos blue galaxies with  $\langle \kappa(\text{C III})_{\text{COS-Halosblue}} \rangle_{0.1} = 0.90 \pm 0.07$  in the COS-Halos survey. While many of the detected C III lines are saturated and therefore only lower limits to the underlying ionic column density N(C III) can be obtained, C III, unlike O VI, does not appear to show a strong bimodality in galaxy haloes.

Similarly, Si III $\lambda$  1206 also appears to be dominant, although the available COS spectra do not provide comparable sensitivities for placing as strong constraints for  $W_r(1206)$  as for C III  $\lambda$  977. Adopting a minimum rest-frame absorption equivalent width of  $W_0 = 0.1$  Å for Si III, we conservatively estimate a mean gas covering fraction of  $\langle \kappa(\text{Si III}) \rangle_{0.1} = 0.4 - 0.7$ , similar to what was found for COS-Halos red galaxies (e.g. Werk et al. 2013).

#### 4.3 Implications

The dominant presence of intermediate ions revealed by C III and Si III absorption constrains the temperature of the absorbing gas to  $T\lesssim 3\times 10^4$  K under either collisional or photoionization scenarios (see e.g. Oppenheimer & Schaye 2013). This is in contrast to  $T\gtrsim 10^{6.5}$  K expected for the hot halo as a result of gravitational heating, and supports a multiphase halo model, in which cool absorbing clouds are pressure-confined in a hot medium. Under a pressure equilibrium, this would imply a density contrast between cool clouds and the hot halo of  $\sim 100:1$ . While dense, cool clouds

are expected to fall in a low-density hot halo, whether or not they can reach the galaxy to fuel star formation depends on the infall time relative to the disruption time (e.g. Maller & Bullock 2004). Under a simple hydrostatic equilibrium assumption, Gauthier & Chen (2011) calculated the minimum mass required for cool clouds to survive thermal conduction from the surrounding hot medium. They found a minimum mass of  $M_{\rm cl} \gtrsim 10^6\,{\rm M}_\odot$ . On the other hand, Huang et al. (2016) reported that the velocity dispersion of Mg II absorbing gas relative to the host LRGs is suppressed in comparison to the expectations from virial motion. These authors attributed the suppressed velocity dispersion to ram-pressure drag force and inferred a maximum cloud mass of  $M_{\rm cl} \approx 5 \times 10^4 \, \rm M_{\odot}$ . While combining these calculations suggests that the majority of cool clouds formed at large distances may not be sufficiently massive to survive the hot halo during infall, we note that the results of these calculations depend sensitively on the model assumptions of the properties of the hot halo and how cool clouds form (e.g. Brighenti & Mathews 2003). Recall that high column density gas is detected at d < 20 kpc around massive lensing galaxies at  $z \approx 0.4$  (e.g. Zahedy et al. 2016, 2017a) and in nearby ellipticals (e.g. Oosterloo et al. 2010; Serra et al. 2012; Young et al. 2014).

We note that while our study focuses entirely on LRGs selected by their quiescent state, the results bear significantly on our overall understanding of feedback mechanisms in galaxy haloes. More than 90 per cent of massive galaxies with  $M_{\rm star} \gtrsim 10^{11} \, {\rm M}_{\odot}$  in the local Universe are observed to contain primarily evolved stellar populations with little ongoing star formation (e.g. Peng et al. 2010; Tinker et al. 2013). The results from our study can therefore be applied broadly to massive haloes of  $M_{\rm star} \gtrsim 10^{11} \, \rm M_{\odot}$ , but in the still higher-mass galaxy cluster regime observations have yielded very different results (see e.g. Yoon et al. 2012; Burchett et al. 2018). In addition, the LRGs also provide a unique sample for identifying additional physical mechanisms, beyond starburst and AGN feedback, that produce the observed optically thick clouds and heavy ions in galactic haloes. A joint study of the ionization state of the gas and the galaxy environment is the next important step for obtaining key insights into these underlying feedback mechanisms.

#### 5 SUMMARY AND CONCLUSIONS

We have carried out an absorption-line survey of cool gas in haloes around a mass-limited sample of LRGs with  $\log M_{\rm star} \geq 11$  at z=0.21-0.55. The LRGs are selected with no prior knowledge of the presence/absence of any absorption features. Our programme is designed such that accurate and precise measurements of  $N({\rm H\,I})$  are possible based on observations of the full hydrogen Lyman series. Our analysis shows that not only are HI absorbers frequently seen at d<160 kpc (or  $d<1/3~R_{\rm vir}$ ) in LRG haloes, but a large fraction (7/16) of these absorbers are also optically thick to an ionizing radiation field with  $\log N({\rm H\,I}) > 17.2$ . In addition, all but one of the LRGs with detected HI absorption also exhibit associated metal-line absorption features, indicating a widespread chemical enrichment in these massive quiescent haloes. The main findings of our survey are summarized below.

- (1) The mean covering fraction of optically thick gas is  $\langle \kappa \rangle_{\rm LLS} = 0.44^{+0.12}_{-0.11}$  at  $d \lesssim 160$  kpc and  $\langle \kappa \rangle_{\rm LLS} = 0.71^{+0.11}_{-0.20}$  at  $d \lesssim 100$  kpc in LRG haloes. These numbers are consistent with the high covering fraction of  $\langle \kappa \rangle_{\rm LLS} = 0.6^{+0.2}_{-0.1}$  observed at  $d \lesssim 80$  kpc from  $L_*$  and sub- $L_*$  star-forming galaxies at  $z \approx 0.2$  from the COS-Halos survey.
- (2) Intermediate ions probed by C III and Si III are the most prominent UV ionic features in these massive quiescent haloes with a

mean covering fraction of  $\langle \kappa(\text{C\,III}) \rangle_{0.1} = 0.75^{+0.08}_{-0.13}$  for  $W_{\rm r}(977) \geqslant 0.1$  Å at d < 160 kpc, comparable to what is seen for C III in  $L_*$  and sub- $L_*$  star-forming and red galaxies but exceeding what is typically observed for strong Mg II or O VI absorbing gas around massive quiescent galaxies.

- (3) While quiescent galaxies exhibit on average fewer strong O vI absorbers of column density log N(O vI) > 14 than star-forming galaxies at d < 160 kpc, the mean gas covering fraction of moderately strong O vI absorbers of log N(O vI) > 13.5 is found to remain high with a mean covering fraction of  $\langle \kappa(\text{O vI}) \rangle_{0.05} = 0.55^{+0.13}_{-0.14}$ .
- (4) The mean covering fraction of Mg II absorbing gas at  $d\lesssim 160$  kpc is found to be  $\langle \kappa({\rm Mg\,II})\rangle_{0.3}=0.27^{+0.16}_{-0.09}$  for  $W_{\rm r}(2796)\geqslant 0.3$  Å, consistent with the mean covering fraction found using the full SDSS LRG sample. For absorbing gas of  $W_{\rm r}(2796)\geqslant 0.1$  Å, the mean covering fraction at d<160 kpc is  $\langle \kappa({\rm Mg\,II})\rangle_{0.1}=0.55^{+0.13}_{-0.14}$ , comparable to what is observed in lower-mass, star-forming galaxies.

In conclusion, the COS-LRG survey has uncovered a high incidence of chemically enriched cool ( $T \sim 10~{\rm K}^{4-5}$ ) gas in massive quiescent haloes hosting LRGs at  $z \approx 0.4$ . A significant fraction of this chemically enriched gas is optically thick to ionizing photons. It shows that massive quiescent haloes contain widespread chemically enriched cool gas. No clear presence of bimodality is found between blue star-forming and red quiescent galaxies in their H<sub>I</sub> gas content or in the incidence of intermediate ions.

#### **ACKNOWLEDGEMENTS**

We thank Joop Schaye and Jonathan Stern for helpful discussions. We thank Michael Rauch for his help in obtaining the MIKE spectra for some of the QSOs presented in this paper. This work is based on data gathered under the HST-GO-14145.01A programme using the NASA/ESA Hubble Space Telescope operated by the Space Telescope Science Institute and the Association of Universities for Research in Astronomy, Inc., under NASA contract NAS 5-26555. HWC and FSZ acknowledge partial support from NSF grant AST-1715692. FSZ acknowledges generous support from the Brinson Foundation and the Observatories of Carnegie Institution for Science during his visit at Carnegie Observatories as a Brinson Chicago-Carnegie pre-doctoral fellow. SDJ is supported by a NASA Hubble Fellowship (HST-HF2-51375.001-A). This research has made use of the Keck Observatory Archive (KOA), which is operated by the W. M. Keck Observatory and the NASA Exoplanet Science Institute (NExScI), under contract with the National Aeronautics and Space Administration.

#### REFERENCES

Adelberger K. L., Steidel C. C., Pettini M., Shapley A. E., Reddy N. A., Erb D. K., 2005, ApJ, 619, 697

Barmby P. et al., 2006, ApJ, 650, L45

Bergeron J., Stasińska G., 1986, A&A, 169, 1

Bernstein R., Shectman S. A., Gunnels S. M., Mochnacki S., Athey A. E., 2003, in Iye M., Moorwood A. F. M., eds, Proc. SPIE Vol. 4841, Instrument Design and Performance for Optical/Infrared Ground-Based Telescopes. SPIE. Bellingham, p. 1694

Blake C., Collister A., Lahav O., 2008, MNRAS, 385, 1257

Blanton M. R., Roweis S., 2007, AJ, 133, 734

Bowen D. V., Chelouche D., 2011, ApJ, 727, 47

Brighenti F., Mathews W. G., 2003, ApJ, 587, 580

Burchett J. N., Tripp T. M., Wang Q. D., Willmer C. N. A., Bowen D. V., Jenkins E. B., 2018, MNRAS, 475, 2067 Chabrier G., 2003, PASP, 115, 763

Charlton J. C., Ding J., Zonak S. G., Churchill C. W., Bond N. A., Rigby J. R., 2003, ApJ, 589, 111

Chen H.-W., 2017a, in Knapen J., Lee J., Gil de Paz A., eds, Astrophysics and Space Science Library, Vol. 434, Outskirts of Galaxies. Springer-Verlag, Berlin

Chen H.-W., 2017b, in Fox A., Dave R., eds, Astrophysics and Space Science Library, Vol. 430, Gas Accretion onto Galaxies. Springer-Verlag, Berlin

Chen H.-W., Gauthier J.-R., Sharon K., Johnson S. D., Nair. P., Liang C. J., 2014, MNRAS, 438, 1435

Chen H.-W., Helsby J. E., Gauthier J.-R., Shectman S. A., Thompson I. B., Tinker J. L., 2010, ApJ, 714, 1521

Churchill C. W., Vogt S. S., 2001, AJ, 122, 679

Conroy C., 2013, ARA&A, 51, 393

Eisenstein D. J. et al., 2001, AJ, 122, 2267

Faucher-Giguère C.-A., 2017, in Fox A., Dave R., eds, Astrophysics and Space Science Library, Vol. 430, Gas Accretion onto Galaxies. Springer-Verlag, Berlin

Faucher-Giguère C.-A., Feldmann R., Quataert E., Kereš D., Hopkins P. F., Murray N., 2016, MNRAS, 461, L32

Ford A. B., Oppenheimer B. D., Davé R., Katz N., Kollmeier J. A., Weinberg D. H., 2013, MNRAS, 432, 89

Foreman-Mackey D., Hogg D. W., Lang D., Goodman J., 2013, PASP, 125, 306

Gauthier J.-R., Chen H.-W., 2011, MNRAS, 418, 2730

Gauthier J.-R., Chen H.-W., Tinker J. L., 2009, ApJ, 702, 50

Gauthier J.-R., Chen H.-W., Tinker J. L., 2010, ApJ, 716, 1263

Hafen Z. et al., 2017, MNRAS, 469, 2292

Hennawi J. F. et al., 2006, ApJ, 651, 61

Hodge J. A., Becker R. H., White R. L., de Vries W. H., 2008, AJ, 136, 1097 Howk J. C. et al., 2017, ApJ, 846, 141

Huang Y.-H., Chen H.-W., Johnson S. D., Weiner B. J., 2016, MNRAS, 455, 1713

Johnson S. D., Chen H.-W., Mulchaey J. S., 2013, MNRAS, 434, 1765

Johnson S. D., Chen H.-W., Mulchaey J. S., 2015a, MNRAS, 452, 2553

Johnson S. D., Chen H.-W., Mulchaey J. S., 2015b, MNRAS, 449, 3263

Johnston H. M., Sadler E. M., Cannon R., Croom S. M., Ross N. P., Schneider D. P., 2008, MNRAS, 384, 692

Lehner N., 2017, in Fox A., Dave R., eds, Astrophysics and Space Science Library, Vol. 430, Gas Accretion onto Galaxies. Springer-Verlag, Berlin

Lehner N., Howk J. C., Wakker B. P., 2015, ApJ, 804, 79 Liang C. J., Chen H.-W., 2014, MNRAS, 445, 2061

Lopez S. et al., 2008, ApJ, 679, 1144

Lundgren B. F. et al., 2009, ApJ, 698, 819

Maller A. H., Bullock J. S., 2004, MNRAS, 355, 694

Montero-Dorta A. D. et al., 2016, MNRAS, 461, 1131

Moustakas J. et al., 2013, ApJ, 767, 50

Muzahid S. et al., 2017, ApJ, 846, L8

Oosterloo T. et al., 2010, MNRAS, 409, 500

Oppenheimer B. D., Crain R. A., Schaye J., 2016, MNRAS, 460, 2157

Oppenheimer B. D., Schaye J., 2013, MNRAS, 434, 1043

Padmanabhan N. et al., 2007, MNRAS, 378, 852

Peng Y.-j. et al., 2010, ApJ, 721, 193

Prochaska J. X., Hennawi J. F., Simcoe R. A., 2013, ApJ, 762, L19

Prochaska J. X., Lau M. W., Hennawi J. F., 2014, ApJ, 796, 140

Prochaska J. X. et al., 2017, ApJ, 837, 169

Rahmani S., Lianou S., Barmby P., 2016, MNRAS, 456, 4128

Rahmati A., Schaye J., Bower R. G., Crain R. A., Furlong M., Schaller M., Theuns T., 2015, MNRAS, 452, 2034

Rao S. M., Turnshek D. A., Briggs F. H., 1995, ApJ, 449, 488

Rao S. M., Turnshek D. A., Nestor D. B., 2006, ApJ, 636, 610

Ribaudo J., Lehner N., Howk J. C., Werk J. K., Tripp T. M., Prochaska J. X., Meiring J. D., Tumlinson J., 2011a, ApJ, 743, 207

Ribaudo J., Lehner N., Howk J. C., 2011b, ApJ, 736, 42

Rigby J. R., Charlton J. C., Churchill C. W., 2002, ApJ, 565, 743

Roseboom I. G. et al., 2006, MNRAS, 373, 349

Rudie G. C. et al., 2012, ApJ, 750, 67

Serra P. et al., 2012, MNRAS, 422, 1835

- Shull J. M., Danforth C. W., Tilton E. M., 2014, ApJ, 796, 49
  Shull J. M., Danforth C. W., Tilton E. M., Moloney J., Stevans M. L., 2017, ApJ, 849, 106
- Sofue Y., 2015, PASJ, 67, 75
- Steidel C. C., Sargent W. L. W., 1992, ApJS, 80, 1
- Stern J., Hennawi J. F., Prochaska J. X., Werk J. K., 2016, ApJ, 830, 87S
  Suresh J., Bird S., Vogelsberger M., Genel S., Torrey P., Sijacki D., Springel
  V., Hernquist L., 2015, MNRAS, 448, 895
- Thom C. et al., 2012, ApJ, 758, L41
- Tinker J. L. et al., 2013, ApJ, 778, 93
- Tojeiro R., Percival W. J., Heavens A. F., Jimenez R., 2011, MNRAS, 413, 434
- Tumlinson J., Peeples M. S., Werk J. K., 2017, ARA&A, 55, 389
- Tumlinson J. et al., 2011, Science, 334, 948
- Tumlinson J. et al., 2013, ApJ, 777, 59
- van de Voort F., 2017, in Fox A., Dave R., eds, Astrophysics and Space Science Library, Vol. 430, Gas Accretion onto Galaxies. Springer-Verlag, Berlin, p. 301
- Vogt S. S. et al., 1994, in David L. C., Eric R. C., eds, Proc. SPIE, Vol. 2198, Symposium on Astronomical Telescopes and Instrumentation for the 21st Century. SPIE, Bellingham, p. 362
- Wakker B. P., Hernandez A. K., French D. M., Kim T.-S., Oppenheimer B. D., Savage B. D., 2015, ApJ, 814, 40

- Watkins L. L., Evans N. W., An J. H., 2010, MNRAS, 406, 264
- Werk J. K., Prochaska J. X., Thom C., Tumlinson J., Tripp T. M., O'Meara J. M., Meiring J. D., 2012, ApJS, 198, 3
- Werk J. K., Prochaska J. X., Thom C., Tumlinson J., Tripp T. M., O'Meara J. M., Peeples M. S., 2013, ApJS, 204, 17
- White M. et al., 2012, MNRAS, 424, 933
- Wild V. et al., 2008, MNRAS, 388, 227
- Wotta C. B., Lehner N., Howk J. C., O'Meara J. M., Prochaska J. X., 2016, ApJ, 831, 95
- Yoon J. H., Putman M. E., Thom C., Chen H.-W., Bryan G. L., 2012, ApJ, 754, 84
- York D. G., Adelman J., Anderson J. E., Jr, et al., 2000, AJ, 120, 1579
- Young L. M. et al., 2014, MNRAS, 444, 3408
- Zahedy F. S., Chen H.-W., Rauch M., Wilson M. L., Zabludoff A., 2016, MNRAS, 458, 2423
- Zahedy F. S., Chen H.-W., Gauthier J.-R., Rauch M., 2017a, MNRAS, 466, 1071
- Zahedy F. S., Chen H.-W., Rauch M., Zabludoff A., 2017b, ApJ, 846, L29 Zheng Z., Coil A. L., Zehavi I., 2007, ApJ, 667, 760
- Zhu G. et al., 2014, MNRAS, 439, 3139

This paper has been typeset from a TEX/LATEX file prepared by the author.